Integrated Microfluidic Device for Efficient Capture of Bacteria and Antimicrobial Susceptibility Testing

Tamer AbdElSalam AbdElFatah AbdElWahab

Master of Engineering

Department of Bioengineering
McGill University
Montreal, Quebec, Canada

November 2019

A thesis submitted to McGill University in partial
fulfillment of the requirements of the degree of
Master of Engineering

Abstract-English

The emergence of antibiotic-resistant bacterial strains poses a major threat to public health worldwide. Currently, drug-resistant pathogens are responsible for hundreds of thousands of annual fatalities. The misuse and overuse of antibiotics is a major promoter for the development of drug-resistant pathogens. Rapid in vitro diagnostic tools are essential to tackle the current drug resistance crisis by allowing rapid detection of pathogen resistance profiles and reducing diagnostic uncertainty and drug misuse.

Here, I present a point of care microfluidic device for capture of bacteria and phenotypic in vitro antibiotic resistance profiling in less than 1 hour. The device employs a resazurin reduction assay, where the color change from dark blue to pink will be monitored in the presence of antibiotic-resistant bacteria. The device contains bacteria capture and color reading chambers. The bacteria capture chamber utilizes a filter with nano-scale pores based on the interaction between pillar arrays and polystyrene beads. The color reading chamber is based on integrated plasmonic nanostructures for sensitive monitoring of color in the presence of resazurin reduction. A computational fluid dynamics simulation was performed to optimize the pillar array design parameters for high throughput capture of bacteria. The efficiency of the capture was validated using fluorescently tagged polystyrene beads and Escherichia coli bacteria. The colorimetric read-out strongly depends on the light absorption and the size of the nanoparticles. Nanoparticles with different diameters (200 nm to 1000 nm) were evaluated for optimizing the optical properties. UV-Vis spectroscopy and bright field microscopy were utilized to determine the optimum nanoparticle diameter for color change detection in different media (air, water, LB, resazurin, and resorufin). Ampicillin-resistant Escherichia coli were used to screen against the efficacy of ampicillin and kanamycin antibiotics. Moreover, we assessed the minimum inhibitory concentration of kanamycin against the Escherichia coli strain. The results were validated by standard antibiotic screening procedures “CLSI”. The device showed rapid phenotypic profiling of antibiotic-susceptibility with quantitative results of different dilution of bacteria and drug concentration.

Keywords: Microfluidics, Bacteria Capture, Antibiotic Resistance Screening, Plasmonics, Nanofilter, Self-assembled Mono Layer, Computational Fluid Dynamics.

Abstract- Français

L'émergence de souches bactériennes résistantes aux antibiotiques constitue une menace majeure pour la santé publique. Actuellement, les agents pathogènes résistants aux médicaments sont responsables de centaines de milliers de décès par an. Le mauvais usage et la surutilisation des antibiotiques sont des facteurs majeurs de développement des agents pathogènes résistants aux médicaments. Des outils de diagnostic in vitro rapides sont essentiels pour faire face à la crise actuelle de la résistance aux médicaments en permettant une détection des profils de résistance des agents pathogènes et en réduisant l'incertitude du diagnostic et le mauvais usage des médicaments.

Je présente ici un dispositif microfluidique au point de service pour la capture des bactéries et le profilage phénotypique de la résistance aux antibiotiques in vitro en moins d'une heure. Le dispositif utilise un test de réduction de la resazurine, où le changement de couleur du bleu foncé au rose sera contrôlé en présence de bactéries résistantes aux antibiotiques. Le dispositif contient des chambres de capture des bactéries et de lecture des couleurs. La chambre de capture des bactéries utilise un filtre avec des pores à l'échelle nanométrique, basé sur l'interaction entre les réseaux de piliers et les billes de polystyrène. La chambre de lecture des couleurs est basée sur des nanostructures plasmoniques intégrées pour un contrôle sensible de la couleur en présence d'une réduction de la resazurine. Une simulation numérique de la dynamique des fluides a été réalisée afin d'optimiser les paramètres de conception des réseaux de piliers pour la capture de bactéries à haut débit. L'efficacité de la capture a été validée en utilisant des billes de polystyrène marquées par fluorescence et des bactéries Escherichia coli. La lecture colorimétrique dépend fortement de l'absorption de la lumière et de la taille des nanoparticules. Des nanoparticules de différents diamètres (200 nm à 1000 nm) ont été évaluées pour optimiser les propriétés optiques. La spectroscopie UV-Vis et la microscopie à champ clair ont été utilisées pour déterminer le diamètre optimal des nanoparticules pour la détection des changements de couleur dans différents milieux. Des Escherichia coli résistants à l'ampicilline ont été utilisés pour vérifier l'efficacité des antibiotiques ampicilline et kanamycine. De plus, nous avons évalué la concentration minimale inhibitrice de la kanamycine par rapport à la souche d'Escherichia coli. Les résultats ont été validés par les procédures standard de dépistage des antibiotiques "CLSI". Le dispositif a montré un profil phénotypique rapide de la sensibilité aux antibiotiques avec des résultats quantitatifs de différentes dilutions de bactéries et concentrations de médicaments.

Mots-clés: Microfluidique, capture de bactéries, dépistage de la résistance aux antibiotiques, plasmonique, nanofiltre, monocouche auto-assemblée, dynamique des fluides computationnelle.

Preface and Author Contributions

Chapter 2 of this thesis has been published in Biomicrofluidics as a research publication titled “A nanofilter for fluidic devices by pillar-assisted self-assembly microparticles” with Tamer AbdElFatah as the first author. All the microfabrication processes were performed at the McGill Nanotools-Microfab. The fluorescent microscopy imaging was conducted using the motorized inverted confocal microscope at the Biological microfluidics research group. Dr. Ayyappasamy Sudalaiyadum Perumal provided help in fluorescently labeled E coli culture and technical advice on the microscope operation.

Chapter 3 of the thesis is adapted from the manuscript under preparation titled “Plasmonic-Enhanced Lab-on-a-Chip Device for Bacteria Drug Susceptibility”. All the microfabrication processes performed at the McGill Nanotools-Microfab. All the bright field microscopy and UV-Vis-Nir spectrometry were conducted at Nanomaterials and Energy Research Center (NanoQAM) at Université du Québec à Montréal (UQAM). The 96 well plate standard antibiotic susceptibility experiment was conducted at Dao Lab in Meakins-Christie Laboratories at McGill University Health Center Research Institute (MUHC). Mahsa Jalali had contributed significantly in platform design and troubleshooting. Mahsa Jalali and Carolina del Real Mata performed the generic procedure for the formation of a self-assembled monolayer of nanoparticles. They contributed to the analysis of Uv-vis spectra and bright field microscopy images. Carolina del Real Mata developed the MATLAB code for automated analysis of the bright field microscopy results. All other material is the original, unpublished, work by the author, Tamer AbdElFatah.

Acknowledgment

I would like to start by thanking my thesis advisor as well as my mentor, Professor Sara Mahshid of Bioengineering Department at McGill University. Throughout my Master's degree, she supported me and guided me in the right direction. She was always there for me whenever I encountered problems or needed advice. A special mention is in place for Mahsa Jalali for her contribution and dedication throughout the project from the design of the experiments, device fabrication and analyzing the platform. Her contributions to the project were crucial for its success. Also, I would like to acknowledge the contribution of Carolina del Real Mata in the fabrication and analysis of plasmonic platforms and conducting different experiments. I am really thankful for the input of Mahsa Jalali and Carolina del Real Mata. My gratitude goes out to all members at Mahshid lab, for their advice, encouragement, and providing a great working environment.

I would like to thank Professor Dan Nicolau and Professor Dao Nguyen for allowing me to conduct part of my experiments in their research facilities. I would like to specifically express my gratitude to Ayyappasamy Sudalaiyadum Perumal who helped me to get on the right foot in my early days at McGill and his continued support in my endless biology-related inquiries. Also, I am grateful for Xavier Elisseeff for his help in teaching bacteria culture procedures and his continues support throughout my master's degree. My heartfelt appreciation goes out to the members at McGill Nanotools-Microfab for their assistance and support in the microfabrication protocols. Also, I would like to acknowledge the support provided by Gwenael Chamoulaud in training and tool troubleshooting for the UV-vis and bright field microscopy.

I am deeply grateful to my previous manager and mentor back at Egypt Prof. Mohamed Ali Basha who introduced me to the fascinating world of microfabrication. I will be forever in your debt for showing me this wonderful world. I would like to thank my Father, mother, and brothers without their support I would have not been where I am today. Last, I would like to thank my wife and son they are my true motivation to push forward and work as hard as I can, staying away from them was nothing short than inferno for me.

Table of Contents

List of Figures and Tables

Chapter 2: A nanofilter for fluidic devices by pillar-assisted self-assembly microparticles

Chapter 3: Plasmonic-Enhanced Lab-on-a-Chip Device for Bacteria Drug Susceptibility (Under preparation)

Appendix A: plasmonic enhanced Lab-on-a-chip device fabrication and characterization

1. Introduction and literature review

1.1. Background

Ever since the discovery of Penicillin by Sir Alexander Fleming, antibiotics played a critical role in fighting bacterial infections. Antibiotics helped to increase the human life span and facilitated the success of other medical procedures as organ transplant, chemotherapy or cardiac surgery.[1] A major challenge facing antibiotics is the development of antibiotic-resistant bacteria. This phenomenon accompanied their use. For example, Methicillin was introduced in 1960 and *Methicillin-resistant Staphylococcus* (*MRSA*) was identified in 1962.[2] Resistance is the result of misuse and over-use of antibiotics. Incorrect prescription of antibiotics exposes patients to their potential side effects with no confirmed therapeutic benefits. Also, bacteria can acquire resistant traits via exposure to sub-therapeutic concentrations of antibiotics.[2] The World health organization (WHO) estimates if no action is taken there will be 10,000,000 annual deaths related to antibiotic-resistant infections by 2050.[3] In response, the WHO proposed a global action plan to face the antimicrobial resistance crisis. The plan includes initiatives for surveillance of antimicrobial incidents in member states and establishing an antibiotic stewardship program for better management of antibiotic administration. Also, it calls for increased research funding to establish improved diagnostic tools.[2,4–6] Better diagnostic tools can effectively reduce the inappropriate use of antibiotics by eliminating diagnostic uncertainty[6]. Current, Antibiotic resistance screening tests are slow requiring approximately 2 days to produce results. General practitioners usually don't resort to diagnostic tools and instead utilize empirical methods to treat patients[7]. For example, microbiological diagnosis was carried out for only 7.6% of 17,435 patients hospitalized with community-acquired pneumonia in the US[6,8]. General practitioners either prescribe a combination of antimicrobial drugs with the aim that one of them might work or prescribe successive treatment courses until reaching an effective one[9]. This subjects the patients to intense and repeated selective pressure encouraging the development of resistant bacteria. Rapid in vitro antibiotic resistance screening tools allows the early determination of the effective treatment course eliminating diagnostic uncertainty, repetitive treatments and associated antibiotic resistance development due to multiple selective pressure cycles.

1.2. Current Antibiotic resistance screening technologies

Traditionally, antibiotic resistance screening has been done using culture methods. These methods depend on culturing bacteria on agar plates with the presence of antibiotic-loaded paper disks. Resistant bacteria will be able to grow in the vicinity of the disks showing a uniform film throughout the plate. In contrast, susceptible bacteria won't be able to grow around the disks and no film is witnessed. These methods usually require 48 hours for assessing the antibiotic resistance profile of the sample bacteria.[10,11] Recently, real-time Polymerase chain reaction (RT-PCR) was introduced for rapid antibiotic screening purposes.[12,13] This technique depends on the duplication of DNA segments of interest. It screens for genes associated with antibiotic resistance and can produce results within 4 hours.[14] GeneExpert by Ceiphed is a current commercial RT-PCR device that can be used to identify bacteria and scan for antibiotic resistance properties.[15,16] It can be implemented in a near point of care setting in central health care facilities/laboratories.[17,18] Unfortunately, this technique has limited applicability in low resource setting environments due to high cost.[19]

There is a need for a rapid point of care diagnostic tools that can operate in a low resource settings environment. Current techniques as culture methods require a long incubation time. Alternatively, PCR techniques provide more rapid detection, yet they require a high initial investment in the establishing of the labs and has high running cost due to the need to use expensive reagents and highly trained personnel.

1.3. Microfluidics for screening bacteria antibiotic resistance properties

Microfluidic technology provides a superb platform to develop a rapid diagnostic tool for bacterial antibiotic resistance screening. Microfluidic devices can handle small fluid volumes ((10^{-18} to 10^{-6} liters), have short analysis time, low sample/reagent consumption and economic manufacturing costs. Microfluidic platforms can screen for antibiotic resistance using multiple techniques as electrochemical sensing[20] or optical detection.[21] Webster et al[22] evaluated the antibiotic susceptibility profile of Pseudomonas aeruginosa biofilms using a microfluidic device. They electrochemically monitored the concentration of electro-active virulence factor pyocyanin as a measure of Pseudomonas aeruginosa cell viability in the presence of colistin sulfate antibiotic. They demonstrated that the peak current and thus pyocyanin was reduced by 68% and 82% after exposure to 16 and 100 mg L^{-1} colistin sulfate indicating reduced cell viability. They

ran the experiments for 45 hours to assess the antibiotic efficacy against the Pseudomonas aeruginosa. Besant et al[20] proposed a more rapid approach. They performed electrochemical measurement of metabolic reduction of resazurin to resorufin by viable bacterial cells in the presence of antibiotics. Using their device, they were able to detect Escherichia coli and Klebsiella pneumoniae as well as detecting their susceptibility profile against ciprofloxacin and ampicillin antibiotics in 1 hour.

Resazurin is a weakly fluorescent dark blue dye that can be reduced through metabolic activities of viable cells to the highly fluorescent and light pink colored resorufin. This is due to the different redox enzymes within the cells as NADH.[23] Jian Lin et al[24] confirmed that resazurin can be used as a cell viability indicator as this reduction reaction can happen only in intracellular environment. Resazurin reduction can be detected via the increase of the fluorescent signal of the resorufin or via colorimetric change from dark blue to pink. Kaushik et al[25] developed a droplet microfluidic system to assess the susceptibility profile of *E. coli* towards gentamicin. They utilized a fluorescent readout for resazurin to determine the *E. coli* viability after gentamicin exposure. They were able to determine the *E. coli* susceptibility profile after 1 hour of incubation. Alternatively, colorimetric based methods are more suited to be applied in point of care/low resource environments as they don't require the use of fluorescent microscopes nor the sophisticated systems required to produce, mix, manipulate and analyze the microfluidic droplets. Reis et al[26] introduced a lab-on-a-stick device for bacterial identification and determining the minimum inhibitory concentration (MIC) of respective antibiotics against them. The lab-on-a-stick device incorporated a colorimetric readout system depending on resazurin reduction assay (blue to pink). They identified E. coli bacteria and identified their MIC against ciprofloxacin and trimethoprim as a proof of concept. The device requires an overnight incubation for MIC detection. Elavarasan et al[27] introduced a more rapid colorimetric approach for assessing bacterial antibiotic susceptibility. They tested various clinical isolates of diarrhoeagenic strains of Escherichia coli, Shigella flexneri, Shigella boydii, and Shigella sonnei. Their platform was able to identify resistant strains and minimum inhibitory concentrations of the antibiotics in 6-7 hours.

An interesting approach to increase the rapidity of colorimetric microfluidic devices is the integration of plasmonic meta-surfaces. Plasmonic meta-surfaces incorporate metallic

nanostructures as nanodisks, ellipses, nanocubes, and multimers. They utilize Plasmon-supported materials such as gold,[28] silver[29] and aluminum.[30] The plasmonic meta-surfaces are optimized to resonate at specific optical frequency thus exhibiting different colors across the visible spectrum.[31] Such structures are patterned using direct-write technologies as e-beam lithography.[32,33] The direct-write technologies suffer from very low throughput and high fabrication costs thus limiting their applicability for mass production situations. Alternative patterning approaches addressing the direct write technologies limitations include sacrificial polymeric nanoparticle templates, controlled phase separation, mesoporous particles assembly, and colloidal particles self-assembly.[34,35] Plasmonic color filters offer high color tunability, sensitive color changing based on medium permittivity and low color degradation rate.[31,32,36,37] Thus, plasmonic meta-surfaces have the potential to sensitively detect small color changes that can be used to increase the rapidity of colorimetric resazurin reduction assays.

Here, I develop an integrated microfluidic device for bacterial capture and phenotypic screening of their antibiotic resistance properties. The device incorporates a bacteria capture chamber and a color reading chamber. First, I developed a filter element based on the interaction between a micropillar array and polystyrene particles (PSP) to confine the bacteria in the capture chamber. I performed a study to optimize the design of the filter element for high bacteria capture efficiency. The bacteria capture was demonstrated using fluorescently tagged *E coli K12* bacteria. Next, I screened for antibiotic resistance properties using Ampicillin resistant *E coli* Bacteria. Different concentrations of the bacteria were challenged using Ampicillin and Kanamycin antibiotics. Moreover, the MIC of Kanamycin was determined to be 8 μg/mL which is in acceptable 2-fold dilatation difference than the value obtained using the gold standard MIC method proposed by Clinical and Laboratory Standards Institute (CLSI). I performed the screening using an integrated plasmonic platform for rapid operation. The results were obtained in less than 1 hour for all bacterial concentrations. For the 5×10^{05} CFU/mL concentration the antibiotic resistance properties were identified after 30 minutes.

2. A nanofilter for fluidic devices by pillar-assisted self-assembly microparticles

Tamer AbdelFatah[1], Mahsa Jalali[1] and Sara Mahshid[1,1)]

[1] *Department of Bioengineering, McGill University, Montreal, QC H3A 0E9, Canada*

We present a nanofilter based on pillar-assisted self-assembly microparticles for efficient capture of bacteria. Under optimized condition, we simply fill the arrays of microscale pillars with submicron scale polystyrene particles to create a filter with nanoscale pore diameter in the range of 308 nm. The design parameters such as the pillar diameter and the inter-pillar spacing in the range of 5 μm- 40 μm are optimized using a multi-physics finite element analysis and computational study based on bi-directionally coupled laminar flow and particle tracking solvers. The underlying dynamics of microparticles accumulation in the pillar array region are thoroughly investigated by studying the pillar wall shear stress and the filter pore diameter. The impact of design parameters, on the device characteristics such as microparticles entrapment efficiency, pressure drop and inter-pillar flow velocity is studied. We confirm a bell-curve trend in the capture efficiency versus inter-pillar spacing. Accordingly, the 10 μm inter-pillar spacing offers the highest capture capability (58.8%), with a decreasing entrapping trend for devices with larger inter-pillar spacing. This is the case that, the 5μm inter-pillar spacing demonstrates highest pillar wall shear stress limiting its entrapping efficiency. As a proof of concept fluorescently labeled *Escherichia coli* bacteria (*E. coli*) were captured using the proposed device. This device provides a simple design, robust operation and ease of use. All of which are essential attributes for point of care devices.

Keywords: nanofilter, micropillar arrays, self-assembly microparticles, multiphysics analysis, microfluidics, bacteria capture

2.1. INTRODUCTION

[1)] Author to whom correspondence should be addressed: E-mail: sara.mahshid@mcgill.ca

Direct and efficient capture of low number of bacteria from body fluids (such as nasal swap) can lead to sensitive detection of bacterial infections. Standard clinical approaches include culture/colony counting techniques, molecular diagnostics based on polymerase chain reaction (PCR)[1] and enzyme linked immunosorbent assay (ELISA).[2] Yet they suffer from being laborious, time-consuming and requiring complex and expensive equipment, long periods to produce results (3-4 days) and 5–7 days for validation.[3]

Compared to classical approaches, micro/nanofluidics offer the ability of precise manipulation of small amounts of fluid (10^{-18} to 10^{-6} liters), short analysis time, low sample/reagents consumption and economically inexpensive test methods.[4–8] More prominently a single microfluidic device can perform a complete set of functions ranging from sample concentration to separation and detection.[9] Current challenges faced by microfluidic technologies are lack of enough sensitivity and throughput for detection of low concentration of analyte to use in point-of-care settings. Recently microfluidic base sample delivery systems are integrated with electrokinetic, centrifugal and magnetic forces or functionalized with biological probes (such as antibody) to address these challenges.

Electro-kinetic microfluidics are strongly dependent on the force experienced by particles carrying net charge in the presence of uniform or non-uniform electric fields.[10–12] This approach has been widely investigated for sample concentration in fluidic devices.[13] Shehadul Islam et al[14] applied electrophoresis for capture and electric lysis of *E. coli* using a nano porous membrane. The device operation was a two steps scheme with a capturing step at lower electric field and an electric lysis step at high electric field. Wen Qiao et al[15] developed a two-stage electrophoretic device for DNA capture and enrichment with enrichment factor of 2790. Foram Madiyar et al[16] proposed a dielectrophoresis (DEP) device based on nano electrode arrays of vertically aligned carbon nanofibers for capture and detection of microbes such as bacteria and viruses with a limit of detection of 1-10 CFU mL^{-1} for viruses. In another attempt del Moral Zamora et al[17,18] proposed an automated DEP device for continuous flow concentration and detection of *E. coli* using impedance measurement technique versus accumulation of bacteria.

Centrifugal microfluidics[19] depend on the centrifugal force generated by a rotating device. It does not require complex pumping system but rather a simple motor and no external

instrumentation. Wiederoder et al[20] proposed a hyper polymer-paper centrifugal device for sample enrichment, mixing and integration of sequential assay steps using *E. coli* bacteria. Another interesting approach by Yuan-Yu Chen et al[21] is based on centrifugal micro flows driven by ionic wind generated near the tip of a corona needle held above a small reservoir. They used their device for pre-concentration and capture of Neisseria and Salmonella bacteria with a limit of detection of 2300 CFU mL^{-1}.

Immunocapture microfluidics[22] depends on specific interaction between target surface marker and an antibody, which is chemically linked to the surface of the substrate providing high specificity towards the target of interest. K. Tsougeni et al[23] proposed a device based on immunoaffinity for capture and thermal lysis of Salmonella in range of 10^2-10^8 cells ml^{-1}. The device featured a plasma treated surface for increasing the surface area and thus the antibody binding capacity.[23] Renjie Wang et al[24] proposed a sandwich immunoassay based on monoclonal goat anti-S. typhimurium antibody for capture of salmonella. Next the captured bacteria were labelled with quantum dots (QD) as a fluorescent marker using QDs–IgG–primary antibody and was detected in situ using a self-assembly light-emitting diode-induced fluorescence detection (LIF) microsystem. This improved the detection sensitivity and the detection limit to 37 CFU ml^{-1}.

Recently, integrated fluidic devices based on nanostructured materials and immunoaffinity detection assays have shown potential applications in high throughput detection of bacteria.[25] We have developed an integrated microfluidic device that combines a nanostructured detection platform with an immunocapture assay for specific capture of *methicillin-resistant-staphylococcus-aureus* (*MRSA*) with a limit of detection of 50 CFU ml^{-1}. [25] The integrated device features a nanoscale filter based on pillar-assisted self-assembly microparticles (PSMP), to avoid escape of bacteria from the analysis chamber.

In particular, filter based microfluidics[26,27] depend on physical constrictions (porous membranes or tightly packed structures or nanopatterned features) to manipulate floating target molecules inside the fluidic device. For example, microscale pillar arrays have been previously used for untangling single DNA molecules (~k base pairs) in micro/nanofluidic devices.[8,28,29] Periodic pillar arrays were used for particle size-based separation through the use of deterministic lateral

displacement arrays.[30,31] This method relies on the fact that the flow path of microparticles between the pillar array region differs depending on the particle size. Huang, L.R., et al.[32] They introduced a mix of 0.8, 0.9 and 1 μm to the device and achieved sorting of different microparticles in 40seconds with a resolution of ~10nanometers.

In this paper, we aim to discuss the design optimization parameters such as the pillar diameter and the inter-pillar spacing for design and fabrication of a PSMP nanofilter. The underlying dynamics of microparticles self-assembly in the region of pillar arrays will be discussed thoroughly by studying the pillar wall shear stress and the filter pore diameter by using a multi-physics finite element analysis study. The proposed PSMP nanofilter is simply assembled by filling the arrays of microscale pillars with micro scale polystyrene particles. The PSMP nanofilter features nanoscale pores with 308nm pore diameter, small enough for the capture of bacteria (such as *E. coli* ~1 μm). Numerical study based on bi-directionally coupled laminar flow and particle-tracking solvers is carried out for studying design optimization parameters and for device performance evaluation. The results are validated with experimental study of *E. coli* capture.

2.2. Experimental Section:

2.2.1. Computational study using COMSOL simulation

The goal of this study is to define the optimum design parameters for pillar-assisted self-assembly microparticles (PSMP) based nanofilter for bacteria capture. We used COMSOL Multiphysics 5.3a software (COMSOL Inc., Burlington, MA) to assess the device performance through finite element analysis simulations. The COMSOL geometry consists of a 2D sketch of the microfluidic chamber (1.5 mm × 3 mm × 50 μm) and arrays of pillars with different design in terms of diameter and inter-pillar spacing. We solved two physics simultaneously based on laminar flow module and particle trajectory tracing module.

In this simulation, a bidirectional coupled particle tracing for fluid flow study was applied. The coupling between microparticles conservation of momentum and Navier-Stokes equation can be

done in COMSOL software by introducing a volume force term (defined by $F_V(r)$) to the latter. Where the volume force is equal in magnitude and opposite in direction to the total drag force (F_D) that the fluid exerts on microparticles. Thus, Navier-Stokes equation for incompressible single-phase fluid in the laminar flow regime can be reduced to:

$$\rho\frac{\partial \boldsymbol{u}}{\partial t} + \rho(\boldsymbol{u} \cdot \nabla)\boldsymbol{u} = \nabla . [-p\boldsymbol{I} + \mu(\nabla \boldsymbol{u} + (\nabla \boldsymbol{u})^T] + \boldsymbol{F} \tag{2.1}$$

$$\rho\nabla \cdot \boldsymbol{u} = 0 \tag{2.2}$$

Where u (SI unit: m/s) is the fluid velocity, p (SI unit: Pa) is the pressure, ρ (SI unit: kg/m^3) is the density, μ (SI unit: Pa s) is the dynamic viscosity, and F (SI unit: N) is the total volume force.

To calculate the contribution of particle motion to the total volume force acting on the fluid (F_v) we calculate the drag force that the fluid exerts on PSB.

$$\frac{d}{dt}(m_p\boldsymbol{v}) = F_D + F_g + F_{ext} \tag{2.3}$$

$$F_D = (\frac{1}{\tau_p})m_p(u - v), \tag{2.4}$$

$$\tau_p = \frac{\rho_p d_p^2}{18\mu} \tag{2.5}$$

Where m_p is the particle mass (SI unit: kg), v is the velocity of the particle (SI unit: m/s), F_D is the drag force (SI unit: N), F_g is the gravitational force (SI unit: N), F_{ext} is any other external force (SI unit: N), τ_p is the particle velocity response time (SI unit: s), u is the fluid velocity (SI unit: m/s), μ is the fluid viscosity (SI unit: Pa s), ρ_p is the particle density (SI unit: kg/m^3), and d_p is the particle diameter (SI unit: m).

Given an array of idealized point masses such that the position vector of the ith particle is denoted q_i (SI unit: m), the volume force at position r is

$$F_V(r) = -\sum_{i=1}^{N} F_{D,i}\delta(r - q_i) \tag{2.6}$$

Where δ is the Dirac delta function, $F_{D,i}$ is the drag force exerted on the ith particle, and N is the total number of particles. The favorable PSP entrapping in the pillar array region conditions is when the total forces opposing the drag force (Volume force and PSPs/pillar interaction forces) are equal to or higher than the drag force. This is the condition when the streamline carrying the PSP moves in the near proximity of the pillar (spacing between streamline and pillar ≈ PSP radius) or ends abruptly at the pillar.

The inlet boundary condition was set to constant velocity (10 μL/min) and one-time initial release of 1000 particles, while the outlet boundary condition was set to constant pressure (atmospheric pressure) with particle freeze condition. All other interfaces were considered as walls using the no slip and freeze boundary conditions. Water was considered as the working fluid. We used a free triangular mesh with total of 27,145 elements.

2.2.2. Design and Fabrication of the microfluidic device

The device was designed using AutoCAD® (Autodesk Inc., CA, USA) and printed on a flexible photomask. Near UV photolithography was used to fabricate the microfluidic features in a SU-8 layer (SU-8 2025, MicroChem Corp., MA, USA) on top of a 4 inch glass substrate, which was then diced to make 9 devices. Next inlet and outlet ports were punched in polydimethylsiloxane (PDMS SYLGARD 184 silicone elastomer, Dow Consumer Solutions, QC, Canada) and bonded to the device surface using established protocols.[25,33] Briefly, PDMS was plasma treated, and put in contact with the SU-8 device under pressure and left for curing overnight at 100 ºC to create an irreversible bond between SU-8 and PDMS.

2.2.3. Fabrication of the pillar-assisted self-assembly microparticles filter

Polystyrene particles (PSP,Fluorescent Nile Red Particles FP-2056-2 ,Spherotech, Lake Forest, IL) were used as the microparticles to fill the micropillar arrays and to create the nanoscale filter. Initially, ethanol was added to the PSP aliquots to stabilize the PSP at the water/air interface and minimize aggregation during the pillar assisted self-assembly process.[34] Next, fluorescent-labled microparticles with 2 μm in diameter were used to experimentally verify the self-assembly process. A 1.22 μl suspension of 2.274×10^8 PSP ml^{-1} in ethanol was pipetted in the inlet port and flown towards the micropillar arrays with an average flow rate of 3.1 μl min^{-1}. Subsequently,

phosphate buffer saline (1X PBS) was pipetted with an average flow rate of 3.1 μl min^{-1} to wash out the excess particles from the bacteria-trapping chamber. Lastly, the device was placed in a vacuum chamber for 90 minutes as a drying step to eliminate the presence of ethanol due to its anti-bacterial properties. After the drying step, the device was ready for bacteria capture process. A motorized inverted confocal microscope (IX83 Olympus) was used to observe the movement of the PSP particles and the self-assembly event. At the end, Mcherry and green fluorescent protein (GFP) labelled *Escherichia coli* K12 bacteria (*E. coli* in LB media) were used to evaluate the device trapping performance and bacteria escape percentage.

2.3. Results and discussion

Figure 2.1a shows a schematic representation of the microfluidic device featuring a region of micro-pillar arrays between a trapping chamber (1.5 mm × 3 mm × 50 μm) and outlet micro-channels (400 μm × 50 μm). The fluids are introduced through an inlet port to the micro-channels and into trapping chamber. At the interface of the trapping chamber and the outlet channel, the micro-pillar arrays filled with PSP to create a nanoscale fluidic region, which trap the bacteria inside the trapping chamber, while allowing the fluid to pass through the pillar arrays and flow through micro-channels into the outlet port.

Figure (2.1b) shows the final prototype (20 mm × 20 mm) consisting of individual fluidic compartments with separate inlets/outlets, featuring small foot print modules for handling multiple sample solution.

We use a two-step process to fabricate the PSMP nanofilter based device. First, the device geometry is defined on SU-8 coated glass substrate using a single mask lithography step and then bonded to a PDMS layer. Figure 2.1c shows the optical image of the micro-pillar arrays patterned on SU-8. Lastly, the micro-pillar arrays are filled with injected PSP, followed by a washing step to create a region of PSMP (Figure 2.1c, inset). The entrapment of PSPs in the pillar array region is resulting from the use of high concentration of PSPs to get entrapped in a structure with a gap bigger than their diameter. This is called the keystone effect[35–37] and was utilized by Ceriotti, L, *et al*[38] to entrap a high concentration of 3 μm particles in a 16 μm gap.

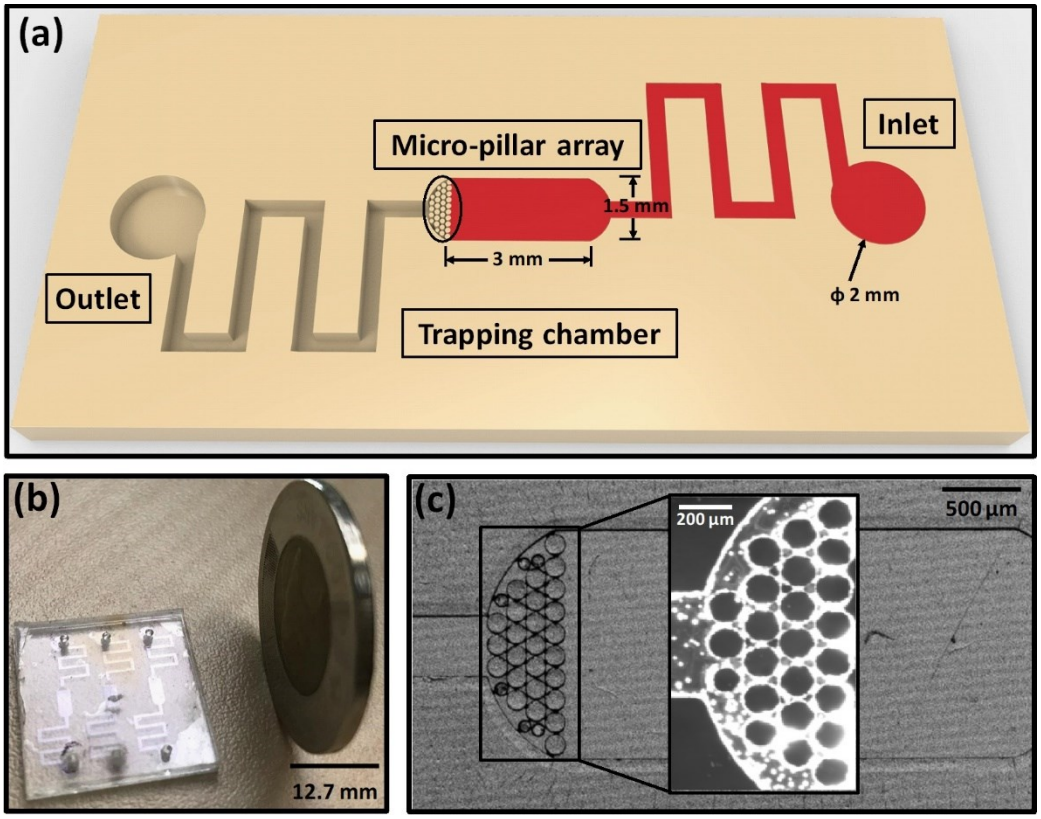

Figure 2. 1 Bacteria trapping device.

(a**)** Schematic representation of bacteria trapping device, consisting of microfluidic channels (400 µm × 50 µm) connecting inlet/outlet ports to a trapping chamber (1.5 mm × 3mm × 50 µm). Micro-pillar arrays are used to trap the target bacteria (*E. coli*). (b) Trapping module (20 mm × 20 mm) containing 3 microfluidic devices. (c) 4X microscopy image of 10 µm inter-pillar spacing trapping device with an inset fluorescent image of PSP filled pillar area.

The entrapped PSP turns the pillar region to a filter with nanoscale pore diameter, which can be simply calculated using hexagonal close packing configuration with packing fraction of 0.74.[39] Figure (2.2a) schematically visualizes red spheres in hexagonal close packing configuration. In this figure, the pore diameter (represented by a blue spherical particle) is determined using the following equation [2.7]:

$$D_p = 0.154 D_s \tag{2.7}$$

Where D_p is the diameter of the pores and D_s is the diameter of the spheres. For 2 µm PSP the pore diameter is 0.308 µm.

Figures 2.2b and 2.2c show the experimental results of entrapped PSPs within the micro pillar arrays under 20X and 40X magnification, respectively. Due to the confined space in designed microfluidic device, there is a limited water/air interface to form PSP self-assembled layer which leads to multi-layered aggregation of PSPs. A mixture of PSP and ethanol was used to enhance stabilization of PSPs at water/air interface to some extent and minimize the aggregation of PSPs.[34] The pore diameter was estimated around 0.319 µm using Image J software, which is in a good agreement with the theoretical value. This confirms our hypothesis for creating a filter with nanoscale pores for capture of microscale biological targets such as bacteria.

In the following section, we use a multi-physics COMSOL simulation based on bi-directionally coupled laminar flow and particle tracing solvers to discuss the optimization parameters such as the pillar diameter and the inter-pillar spacing and to evaluate the underlying dynamics of PSP self-assembly in the pillar arrays.

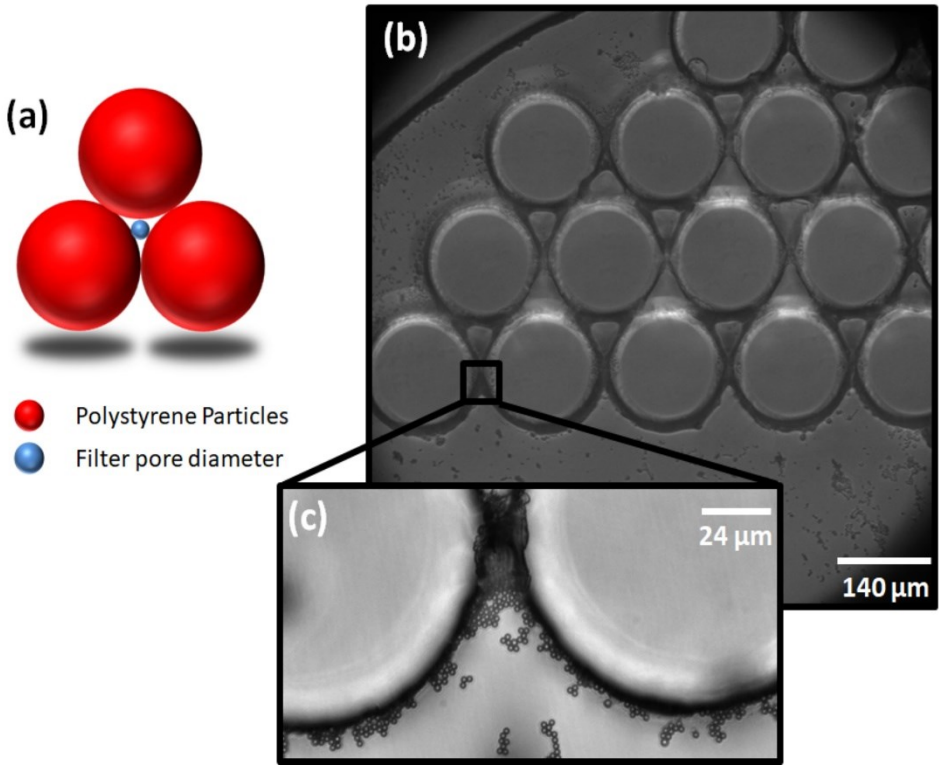

Figure 2. 2. PSP accumulation dynamics and filter pore diameter estimation.

(a) A representation of accumulated PSP (red spheres) in hexagonal close packing structure with the blue sphere representative of the pore diameter. (b-c) Microscopic image of entrapped PSP in pillar arrays area with 20X and 40X zoom respectively.

2.3.1. Computational study of the fluidic characteristics

We applied a 2D COMSOL multi-physics simulation to assess PSP entrapping performance for different device geometries. Figures (2.3a-2.3e) represent the proposed geometries with different inter-pillar spacing of 5, 10, 15, 20 and 40 µm, respectively. We chose the current dimensions for favorable fabrication conditions. Using smaller inter-pillar spacing would inherently introduce more challenging fabrication requirement, due to higher aspect ratio structures. We evaluate the impact of the design parameters on the device characteristics such as 1) PSP entrapment efficiency, 2) pressure drop and 3) inter-pillar flow velocity.

First, we study the effect of inter-pillar spacing on the pressure drop for different geometries. Figure (2.4a) shows the pressure drop profile within the device and the micro pillar arrays. From the pressure profile in Figure 2.4a, it is clear that the region of pillar arrays represents the highest flow resistance and pressure drop. Figure (2.4b) shows the pressure distribution inside the pillar arrays along a cut line in the middle of the geometry (represented by a red line in figure (2.4d)). The plot shows nearly constant pressure values before and after the pillar arrays, and an abrupt steep pressure drop (~ 90% of the overall pressure drop) within the boundaries. Figure (2.4c) represent the overall pressure drop for different inter-pillar spacing, ranging from 9870 Pa for 5 µm inter-pillar spacing to 85.9 Pa for 40 µm inter-pillar spacing.

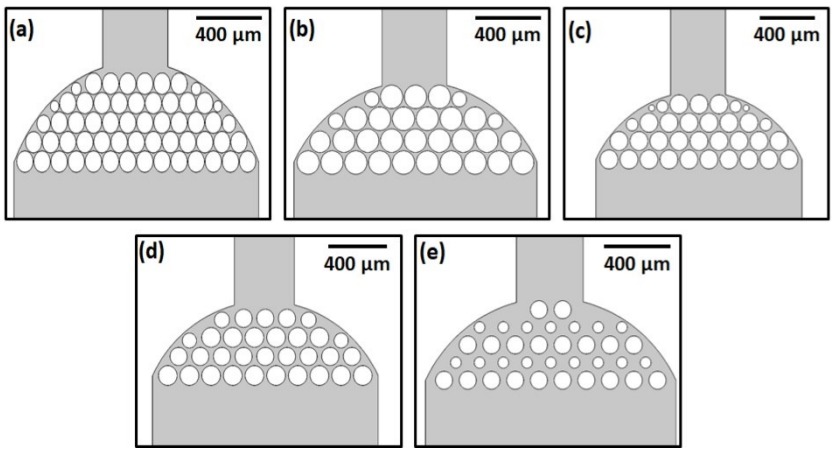

Figure 2. 3 Different proposed device geometries.

(a-e) 2D models for 5, 10, 15, 20 and 40 µm inter-pillar array spacing respectively. Different inter-pillar arrays spacing geometries are investigated using numerical simulation software package COMSOL Multiphysics to establish the optimum design for the micro-pillar arrays.

Second, we study the effect of inter-pillar spacing on the inter-pillar velocity. Figure (2.4d) shows the streamlines in the pillar arrays extracted from COMSOL simulation. The fluorescent image in Figure (2.4e) experimentally shows the flowing pattern of PSP through the analysis well and the pillar region, which is in agreement with the numerical simulation result presented in figure (2.4d). The higher streamline density inside the pillar region (Figure 2.4d) indicates higher flow velocity, which is due to the geometrical constrains. The laminar flow regime can be observed by the parallel streamlines in both numerical and experimental results. Figure 2.4f represents a 10 to 80-fold increase in the velocity -compared with inlet velocity- for different geometries with inter-pillar spacing from 40 µm to 5 µm, respectively.

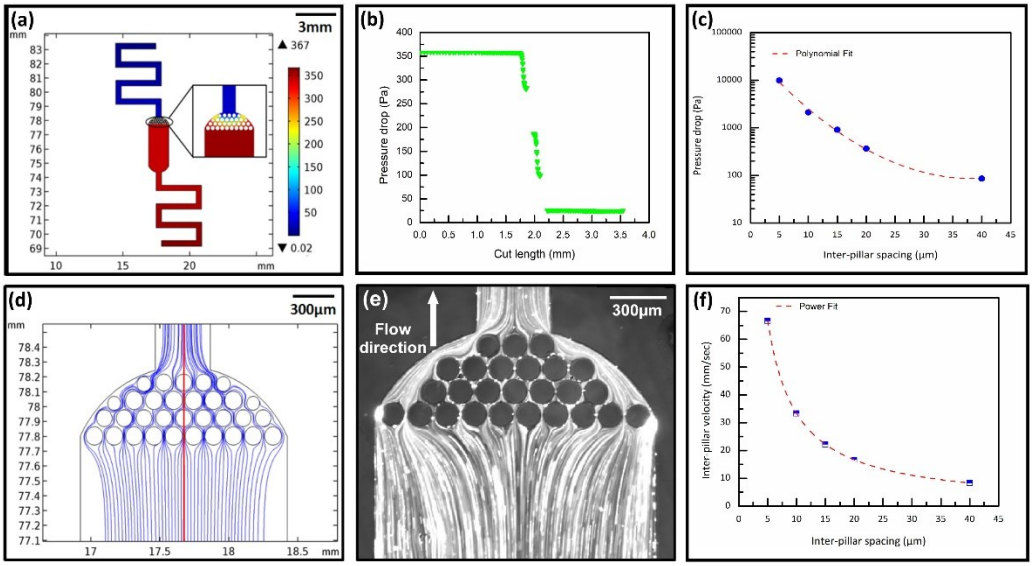

Figure 2. 4 Device pressure and velocity characteristics.

(a) Total pressure drops versus different inter-pillar spacing geometries. Smaller inter-pillar spacing is associated with higher pressure drop due to higher flow resistance. (b) pressure drop across the pillar arrays as shown by Pressure distribution versus cut line length (shown in 4d as red line) plot. (d) Fluid streamlines inside the pillar arrays. Fluid velocity is generally at much higher speeds in the pillar arrays region due to constricted area. This is evident by higher streamline density in the constricted area. (e) 4X fluorescent microscopy image of PSP filling the pillar region. The experimental results show a good agreement with the flow pattern estimated by the numerical simulation. (f) Inter-pillar flow velocity for different inter-pillar spacing geometries. Higher fluid velocities are associated with smaller inter-pillar spacing.

2.3.2. Study the device PSP entrapment performance

The optimum design parameters such as pillars dimension and inter-pillar spacing are determined by using COMSOL simulation results of PSP entrapping regime. We define “particle

entrapment" parameter to determine the efficiency of entrapping PSP in the pillar arrays according to equation [2.8]. A counter was used to count the PSP escaping the pillar area.

$$Particle\ entrapment\ = \frac{Total\ released\ particles - Escaped\ particles}{Total\ released\ particles} \times 100 \qquad (2.8)$$

Figure 2.5a shows the total number of PSP captured by each row within the pillar arrays for different device geometries. We observe similar trend for all the proposed geometries, in which the upstream rows can capture more PSP compared to the further downstream rows.

The particle entrapment efficiency results (calculated from Equation 2.8) in Figure 2.5b show a bell-shaped trend between the number of entrapped PSP versus inter-pillar spacing. As shown in Figure (2.5b) under the simulation conditions it is evident that the 10 µm inter-pillar spacing has the highest particles retention capabilities (58.8%) followed by the 15 µm geometry (53.9%). Contrary to the initial assumption, the 5 µm model with the smallest inter-pillar spacing does not represent the highest particle entrapment efficiency (only 50% particle entrapment efficiency).

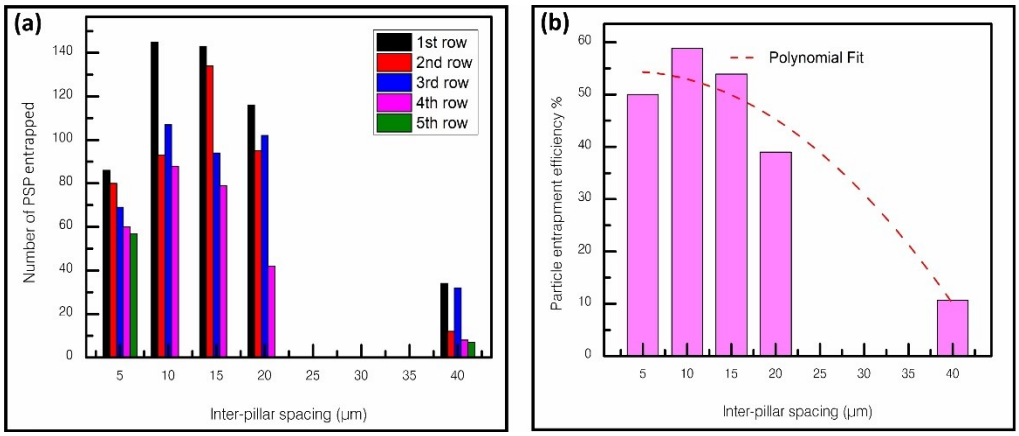

Figure 2. 5 The number and efficiency of entrapped PSP versus different devices.

(a) Number of PSP entrapped per row for different device geometries. There is a consistent pattern for higher PSP entrapping for upstream rows than downstream rows for all proposed designs. (b) Particle entrapment efficiency for different device geometries. 10 µm and 15 µm inter-pillar spacing devices exhibits the highest particle entrapping efficiency making them the optimum designs.

We also numerically studied the transient time (defined as the time needed to reach steady state condition for filling the pillars) versus inter-pillar spacing as shown in Figure 2.6. All the proposed geometry represents short transient time and reach the steady state in few seconds.

Figure (2.6, inset) compares the numerical results of steady state (filled) PSMP nanofilter for 10 µm, 5 µm and 20 µm inter- pillar spacing geometries.

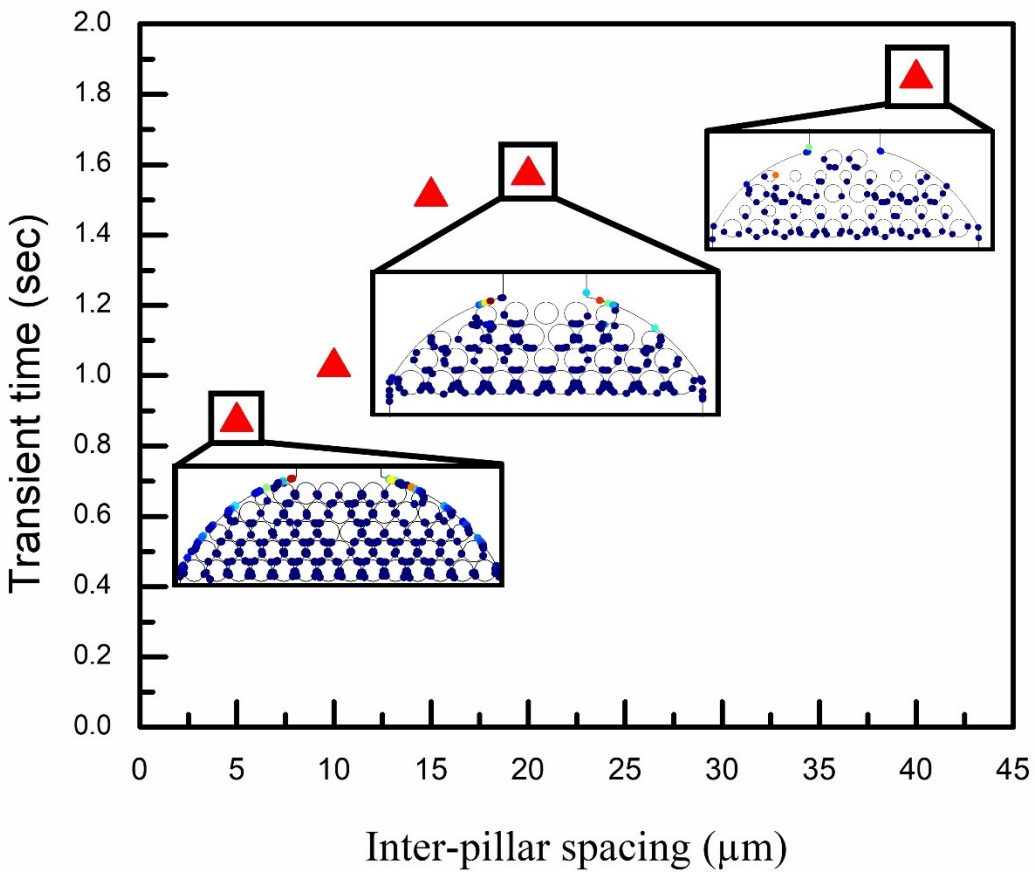

Figure 2. 6 Transient time of filling the pillars for different geometries.

Plot of time needed to reach steady state condition for filling the pillars for different inter-pillar spacing geometries. The designs exhibit a rapid operation reaching steady state in approximately 2 seconds. Figure 2.6 inset comparison of numerical results of steady state for different PSMP nanofilter geometries.

We studied the reason behind the deteriorating performance of the pillars with 5 µm inter-pillar spacing by looking at the forces applied to PSP between pillars as described below. Figure 7a shows a PSP with diameter r, flowing along a streamline. The figure shows a constriction area between two pillars with a pressure driven fluid, moving with velocity U (Z) and exerting viscous friction force F_{vf} on the pillar walls. The friction force is acting on the pillar walls and the entrapped PSP, and can be calculated using the following set of equations:

$$F_{vf} = \tau_{wall} \times A_{pillar} \tag{2.9}$$

$$\tau_{wall} = 2\eta G_m \tag{2.9a}$$

$$G_m = \frac{4\,U_m}{H} \tag{2.9b}$$

$$U_m = 1.5\,U_{ave} \tag{2.9c}$$

Where F_{vf} is the viscous friction force, τ_{wall} is the shear stress induced by the fluid flow at the pillar walls, A_{pillar} is the circumference area of the pillars, η is the fluid viscosity, G_m is the maximum shear rate at the pillar wall,[40] U_m is the maximum velocity of cross-section flow, H is the inter-pillar thickness and U_{ave} is the average velocity of cross-section flow.

We establish the viscous friction force (F_{vf}) values for different device inter-pillar spacing and present the results in Figure 7b. We first start by calculating the average flow velocity between the pillars (U_{ave}) by dividing the flow rate by the cross-section area between the pillars (inter-pillar spacing × pillar height). Next the maximum flow velocity (U_m) between the pillars is evaluated using equation (2.9c). Using the obtained U_m, we estimate the maximum shear rate at the pillar wall (G_m). The pillar wall shear stress (τ_{wall}) is evaluated using equation (2.9a) by substituting the calculated value of G_m and the fluid dynamic viscosity. Lastly the shearing viscose friction force is calculated by multiplying τ_{wall} and the Pillars surface area. Since each device contained different pillar diameters the total pillar surface area is the summation of their surface areas as shown by $\sum \pi n_D D\,L$, where n_D is the number of pillars having a certain diameter (D), D is the pillar diameter extracted from COMSOL geometry in Figure 2.3, and L is the pillar height (50 μm). Figure 2.7c and 2.7d represents the total pillar area and the wall shearing stress (τ_{wall}) versus inter-pillar spacing, respectively.

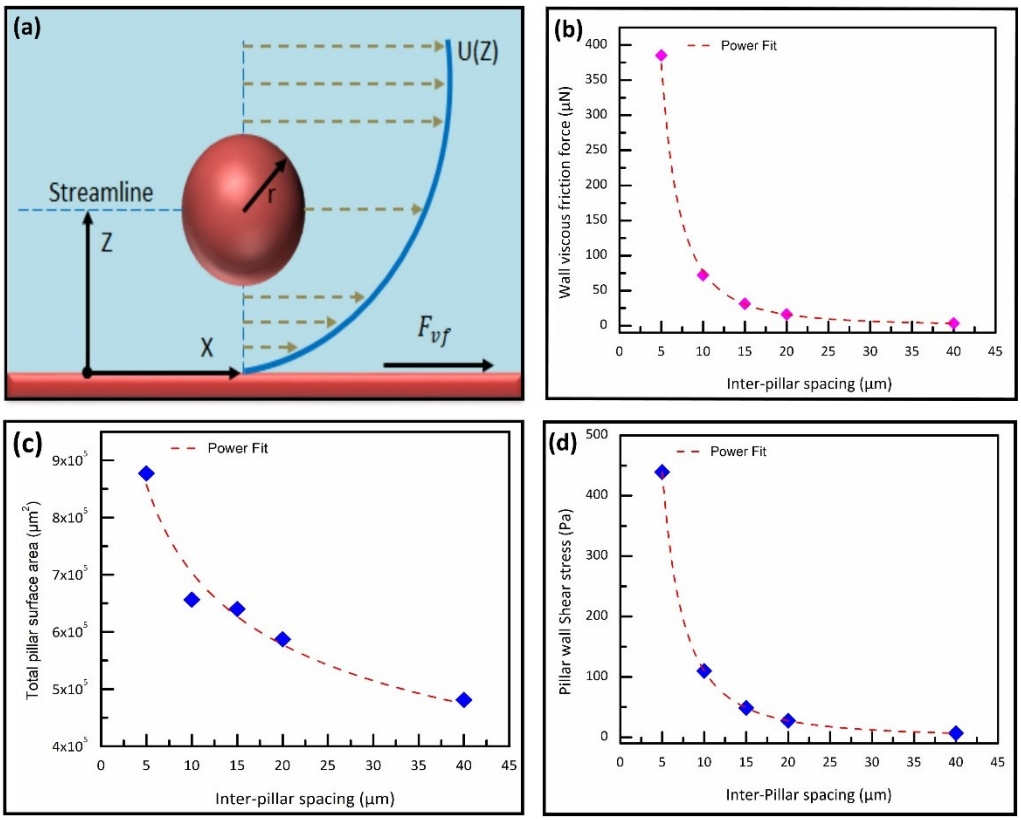

Figure 2. 7 Effect of inter-pillar spacing on PSP filling and shearing forces.

(a) A representation of a PSP with radius r flowing along a stream line in a pressure driven flow and at a distance z from the side wall with viscous friction force F_{vf} applied by the moving fluid on the stationary wall. (b) Wall viscous friction forces for different device designs. It is noted that the 5 μm geometry exhibits the highest wall viscous friction force resulting in less entrapping of PSP, this is due to high shearing stresses and higher surface area compared to other designs. (c) Total pillar surface area and (d) Pillar wall shear stress for different device designs.

According to the figures, the 5 μm inter- pillar spacing design exhibits both the highest shear stress values and the highest total pillar areas (877033.4 μm^2). The combination of which limits the PSP entrapment efficiency by introducing 5 times higher shear viscous friction force than the next design (10 μm inter- pillar spacing) and 117 times higher shear viscous friction force than the design with the least shear forces (40 μm inter- pillar spacing), as shown by Figure (2.7b). There is a general trend of reduction in wall shear forces with increasing the inter-pillar spacing. This is due to the reduction in the maximum flow velocity by increasing the constriction area. Also, a reduction trend of total pillar area for wider spacing designs is observed. The combination of which lead to a reduction in friction force with wider pillar spacing.

We also studied the relation between the pillar size and the average number of entrapped PSP (see Figure 2.8). From the Figure 2.7c, the 10 μm and 15 μm designs featured 6.56×10^5 μm^2

and 6.4 × 10^5 µm^2 total pillar surface area, respectively (varying from 8.77 × 10^5 µm^2 to 4.81 × 10^5 µm^2). Figure 2.8a demonstrates the calculated average PSPs entrapped per pillar for different pillar diameters, while Figure 2.8b shows the total pillar surface area for different designs versus average captured PSP per pillar indicating the average PSB captured per pillar for different device designs. In order to observe the effect of changing pillar diameter on PSP entrapment, we studied a general trend of higher PSP entrapment with larger pillar diameter except for the pillar with 137.2 µm which is associated with the 5 µm inter-pillar spacing design (this design exhibited higher wall shear forces limiting the PSPs entrapment). We confirmed the result trend through plotting total pillar surface area for different designs versus average PSP entrapped per pillar (Figure 2.8b), which shows a general trend of higher PSP entrapment with larger total pillar surface area. As previously discussed, the only exception is the 5 µm design, which is associated with high wall viscous shearing forces. In conclusion, the 10 µm and 15 µm devices are the optimum designs.

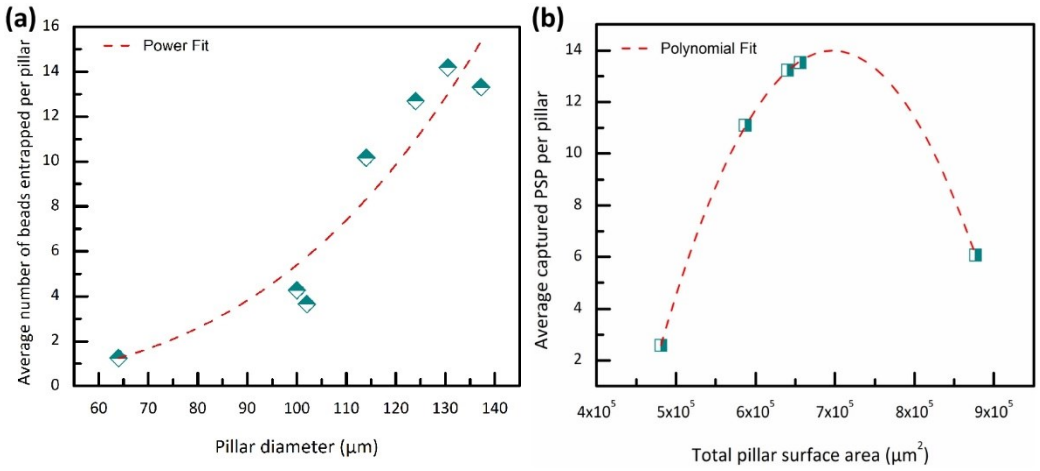

Figure 2. 8 Relation between the pillar size and the average captured PSP per pillar.

(a) Average number of PSPs entrapped per pillar for different pillar diameters. There is a general trend of higher average PSPs entrapping per pillar for bigger diameter pillars. (b) Total pillar surface area versus average captured PSP per pillar. Larger total pillar surface area devices exhibit higher PSP entrapped per pillar, the only exception of this the 5 µm device which is affected by high pillar wall shear stresses compromising its PSP entrapping performance.

2.3.3. Proof of concept bacteria capture

The bacteria trapping performance of the device was experimentally evaluated as a proof of concept. *E. coli* samples were received from culture media and were splitted into aliquots with

15×10^3 CFU ml^{-1}, 3×10^5 CFU ml^{-1} and 3×10^7 CFU ml^{-1} concentrations that was identified by spectrophotometer. For bacteria trapping and visualization experiments a 5 µL of 3×10^7 CFU ml^{-1} *E. coli* sample was pipetted to the device at an average flow rate of 4µl min^{-1}. While for estimating bacteria escaping percentage a 2 µL of *E. coli* sample was pipetted to the device at an average flow rate of 4µl min^{-1} and the downstream of the filter was imaged and analysed using Image J software. Figure (2.9a) is a 4X fluorescent microscopy image of a PSP filled pillar array with a 40X microscopic inset image showing the pattern of the entrapped PSP. The high-resolution microscopy image of PSP entrapment shows a minimized aggregation of the PSP layer which was achieved by treatment of PSPs with ethanol prior to injection. The pillar-assisted self-assembly microparticles filter shows the predicted entrapping pattern as predicted by the numerical simulation result (figure (2.9b)). Figure (2.9c) is 4X fluorescent microscopy image of captured *E. coli* bacteria, a virtual colouring scheme was applied for better representation of the capturing event. *E. coli* bacteria tagged with green fluorescence protein (GFP) were used to confirm the successful capture of bacteria and differentiate between bacteria and PSP in fluorescence microscopy images. Figure (2.9d) is a binary image showing the interface of PSMP nanofilter and trapping chamber. The Binary image is the result of combining red and green channel fluorescence images for the same region. The GFP tagged *E. coli* bacteria were observed as green signals in the binary image, thus we were able to identify the presence of both PSP and *E. coli* bacteria and differentiate between them. The device was able to perform efficient capture of *E.coli*. Figure (2.9e) plots the escaping bacteria for different bacteria concentration. The device exhibits low bacteria escape as shown by the curve with only 3.57% bacteria escaping at bacteria concentration of 3×10^7CFU ml^{-1}.

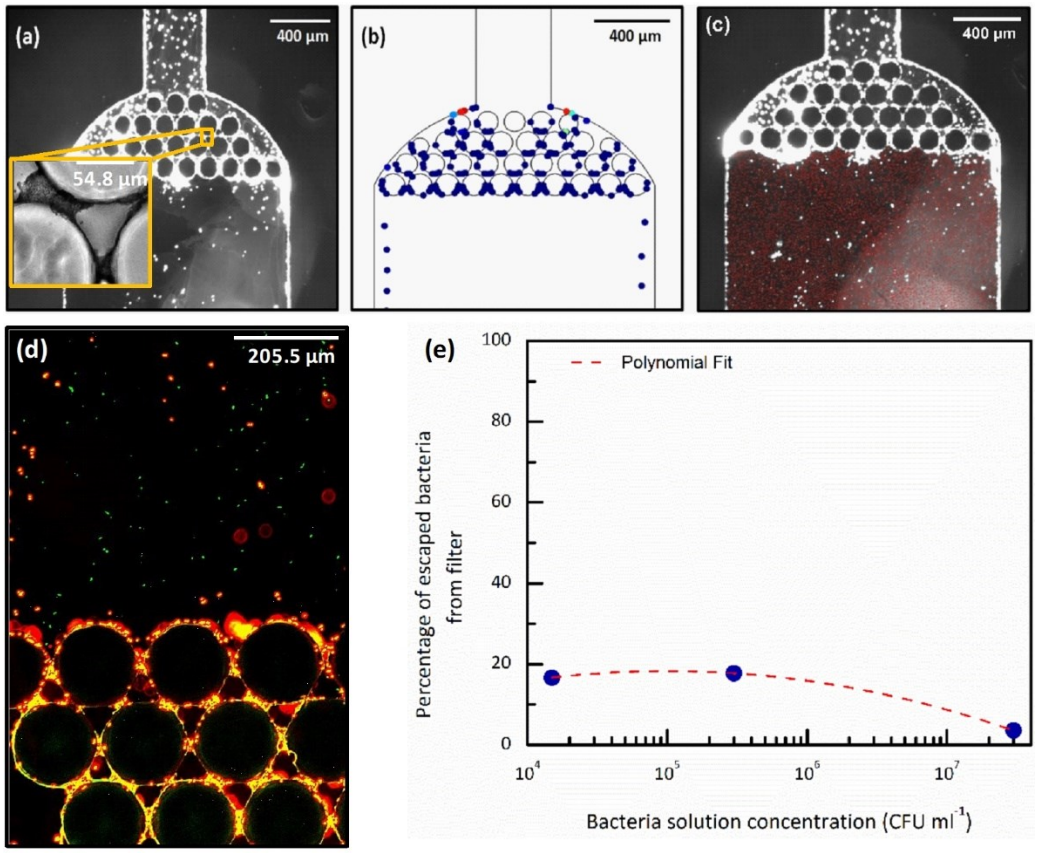

Figure 2. 9 PSP self-assembly and bacteria trapping.

(a) 4X fluorescent images of entrapped PSP and 40X microscopic image inset showing entrapped PSP. The entrapped PSP were pipetted to the device and subsequently undergone a washing step using PBS. (b) PSP entrapping in device as predicted by numerical simulation. The experimental results are in a good agreement with the numerical predictions shown in previously. (c) 4X fluorescent image of trapped *E coli*. Bacteria showing efficient bacteria capturing, note a virtual colouring scheme was applied to highlight trapped bacteria for better result representation. (d) 10X fluorescent image (binary image) for PSP filled pillar region trapping *E.coli*. bacteria (shown in green). The image is the result of combination of red and green channel images for the same region, note that the PSPs appear in yellow colour as they have a wide emission spectrum thus they appear in both red and green images, while, GFP labelled *E.coli* bacteria appears only in green colour. (e) Percentage of bacteria escaping the filter versus bacteria concentration (CFU ml^{-1}). The plot shows the low bacteria escape for different concentrations.

2.4. Conclusion

We introduced a PSMP nanofilter based microfluidic device for bacteria trapping. The device features the integration of micro-pillar arrays with polystyrene Particles (PSP) to build a nano/micro interface for bacteria trapping. Numerical simulations were carried out to thoroughly discuss the device optimization parameters and the dynamics controlling the PSP entrapping regime. The design parameters such as the pillar diameter and the inter-pillar spacing in the range of 5 µm- 40 µm were optimized using multiphysics COMSOL simulation coupling bi-

directionally laminar flow and particle tracking solvers. Accordingly, the 10 μm inter-pillar spacing offers the highest PSP capture capability (58.8%), with a decreasing PSP entrapping trend for devices with larger inter-pillar spacing, suggesting a bell-curve trend in the capture efficiency of the pillar arrays versus inter-pillar spacing. The device was simply fabricated by a single step lithography process of SU-8 coated glass substrate followed by introducing PSP under optimized condition to create PSMP nanofilter. The pillar-assisted self-assembly microparticle filter features nanoscale pore size of 0.308μm to avoid bacteria (~1 μm) escaping the trapping chamber, which was experimentally confirmed for *E. coli* bacteria.

2.5. Acknowledgment

The authors thank Faculty of Engineering at McGill University and Natural Science and Engineering Research Council of Canada (NSERC, G247765) for financial support. M.J. is grateful for MEDA award by the Faculty of Engineering at McGill University and T.A.F. is grateful for STEM scholarship from Abdulla Al Ghurair Foundation for Education. The authors acknowledge Nanotools-Microfab and the Facility for Electron Microscopy Research at McGill University and the Department of Bioengineering Research Facilities. The authors would like to thank CMC Microsystems for CAD tools support. In addition, authors would like to thank Ayyappasamy Sudalaiyadum Perumal for assistance in bacteria culture and Gen Tsutsumi for assisted in COMSOL simulation.

2.6. References

1. Li, M. *et al.* Simultaneous detection of four different neuraminidase types of avian influenza A H5 viruses by multiplex reverse transcription PCR using a GeXP analyser. *Influenza Other Respi. Viruses* **10**, 141–149 (2016).
2. Teoh, B. T. *et al.* The Use of NS1 Rapid Diagnostic Test and qRT-PCR to Complement IgM ELISA for Improved Dengue Diagnosis from Single Specimen. *Sci. Rep.* **6**, 1–8 (2016).
3. Wagenlehner, F. M. E., Pilatz, A. & Weidner, W. Urosepsis - From the view of the urologist. *Int. J. Antimicrob. Agents* **38**, 51–57 (2011).
4. Abdulwahab, S. *et al.* Towards a personalized approach to aromatase inhibitor therapy: a digital microfluidic platform for rapid analysis of estradiol in core-needle-biopsies. *Lab Chip* **17**, 1594–1602 (2017).
5. Gnyawali, V., Saremi, M., Kolios, M. C. & Tsai, S. S. H. Stable microfluidic flow

focusing using hydrostatics. *Biomicrofluidics* **11**, (2017).
6. Ghaemi, R., Rezai, P., Nejad, F. R. & Selvaganapathy, P. R. Characterization of microfluidic clamps for immobilizing and imaging of Drosophila melanogaster larva's central nervous system. *Biomicrofluidics* **11**, (2017).
7. Besant, J. D., Sargent, E. H. & Kelley, S. O. Rapid electrochemical phenotypic profiling of antibiotic-resistant bacteria. *Lab Chip* **15**, 2799–2807 (2015).
8. Mahshid, S. *et al.* Development of a platform for single cell genomics using convex lens-induced confinement. *Lab Chip* **15**, 3013–20 (2015).
9. Zhao, C., Ge, Z. & Yang, C. Microfluidic Techniques for Analytes Concentration. *Micromachines* **8**, 28 (2017).
10. Hamada, R. *et al.* A rapid bacteria detection technique utilizing impedance measurement combined with positive and negative dielectrophoresis. *Sensors Actuators, B Chem.* **181**, 439–445 (2013).
11. Puchberger-Enengl, D. *et al.* Microfluidic concentration of bacteria by on-chip electrophoresis. *Biomicrofluidics* **5**, (2011).
12. Zhang, W. & Radadia, A. D. Toward a Boron-Doped Ultrananocrystalline Diamond Electrode-Based Dielectrophoretic Preconcentrator. *Anal. Chem.* **88**, 2605–2613 (2016).
13. Mahshid, S. *et al.* Transverse dielectrophoretic-based DNA nanoscale confinement. *Sci. Rep.* **8**, 1–12 (2018).
14. Islam, S. *et al.* Electrophoretic Concentration and Electrical Lysis of Bacteria in a Microfluidic Device Using a Nanoporous Membrane. (2017). doi:10.3390/mi8020045
15. Qiao, W. *et al.* A two-stage electrophoretic microfluidic device for nucleic acid collection and enrichment. *Microfluid. Nanofluidics* **20**, 1–9 (2016).
16. Madiyar, F. R., Syed, L. U., Arumugam, P. & Li, J. Electrical capture and detection of microbes using dielectrophoresis at nanoelectrode arrays. in *ACS Symposium Series* **1143**, 109–124 (2013).
17. del Moral Zamora, B. *et al.* Dielectrophoretic concentrator enhancement based on dielectric poles for continuously flowing samples. *Electrophoresis* **36**, 1405–1413 (2015).
18. del Moral-Zamora, B. *et al.* Combined dielectrophoretic and impedance system for on-chip controlled bacteria concentration: Application to Escherichia coli. *Electrophoresis* **36**, 1130–1141 (2015).
19. Yan, H. *et al.* Multiplex detection of bacteria on an integrated centrifugal disk using bead-beating lysis and loop-mediated amplification. *Sci. Rep.* **7**, 1–11 (2017).
20. Wiederoder, M. S. *et al.* Novel functionalities of hybrid paper-polymer centrifugal devices for assay performance enhancement. *Biomicrofluidics* **11**, (2017).
21. Chen, Y. Y. *et al.* Corona-induced micro-centrifugal flows for concentration of Neisseria and Salmonella bacteria prior to their quantitation using antibody-functionalized SERS-reporter nanobeads. *Microchim. Acta* **184**, 1021–1028 (2017).
22. Li, H.-Y. *et al.* Micropillar array chips toward new immunodiagnosis. *Lab Chip* **10**, 2597–604 (2010).
23. Tsougeni, K. *et al.* Plasma nanotextured polymeric lab-on-a-chip for highly efficient bacteria capture and lysis. *Lab Chip* **16**, 120–131 (2016).
24. Wang, R. *et al.* Immuno-capture and in situ detection of Salmonella typhimurium on a novel microfluidic chip. *Anal. Chim. Acta* **853**, 710–717 (2015).
25. Jalali, M. *et al.* A Hierarchical 3D Nanostructured Microfluidic Device for Sensitive Detection of Pathogenic Bacteria. *Small* 1801893 (2018). doi:10.1002/smll.201801893

26. Chang, C. H. & Yang, R. J. Enhanced sample preconcentration in microfluidic chip using graphene oxide–Nafion membrane. *Microfluid. Nanofluidics* **20**, 1–9 (2016).
27. Tian, F., Lyu, J., Shi, J., Tan, F. & Yang, M. A polymeric microfluidic device integrated with nanoporous alumina membranes for simultaneous detection of multiple foodborne pathogens. *Sensors Actuators, B Chem.* **225**, 312–318 (2016).
28. Ahamed, M. J. *et al.* Continuous Confinement Fluidics: Getting Lots of Molecules into Small Spaces with High Fidelity. *Macromolecules* **49**, 2853–2859 (2016).
29. Zimny, P., Juncker, D. & Reisner, W. Hydrogel droplet single-cell processing: DNA purification, handling, release, and on-chip linearization. *Biomicrofluidics* **12**, (2018).
30. Feng, S. L., Skelley, A. M., Anwer, A. G., Liu, G. & Inglis, D. W. Maximizing particle concentration in deterministic lateral displacement arrays. *Biomicrofluidics* **11**, (2017).
31. Holm, Stefan H.; Beech, Jason P.; Barrett, Michael P.; Tegenfeldt, J. O. Separation of parasites from human blood using deterministic lateral displacement †. *Lab Chip* 1326–1332 (2011). doi:10.1039/c0lc00560f
32. Huang, L. R., Cox, E. C., Austin, R. H. & Sturm, J. C. Continous particle separation through deterministic lateral displacement. *Science (80-.).* **304**, 987–991 (2004).
33. Zhang, Z., Zhao, P., Xiao, G., Watts, B. R. & Xu, C. Sealing SU-8 microfluidic channels using PDMS. *Biomicrofluidics* **5**, (2011).
34. Dai, Z., Li, Y., Duan, G., Jia, L. & Cai, W. Phase Diagram , Design of Monolayer Binary Colloidal Crystals , and Their Fabrication Based on Ethanol-Assisted Self-Assembly at the Air / Water Interface. *ACS Nano* 6706–6716 (2012). doi:10.1021/nn3013178
35. Nagy, A. & Gaspar, A. Packed multi-channels for parallel chromatographic separations in microchips. *J. Chromatogr. A* **1304**, 251–256 (2013).
36. Beech, Jason P.; Tegenfeldt, J. O. Microfluidics Separation and Analysis of Biological Particles. (Lund university, 2011).
37. McGrath, J., Jimenez, M. & Bridle, H. Deterministic lateral displacement for particle separation: A review. *Lab on a Chip* **14**, 4139–4158 (2014).
38. Ceriotti, L., De Rooij, N. F. & Verpoorte, E. An integrated fritless column for on-chip capillary electrochromatography with conventional stationary phases. *Anal. Chem.* **74**, 639–647 (2002).
39. Greenwood, R., Luckham, P. F. & Gregory, T. The effect of diameter ratio and volume ratio on the viscosity of bimodal suspensions of polymer latices. *J. Colloid Interface Sci.* **191**, 11–21 (1997).
40. Asmolov, E. S., Dubov, A. L., Nizkaya, T. V., Harting, J. & Vinogradova, O. I. Inertial focusing of finite-size particles in microchannels. *J. Fluid Mech.* **840**, 613–630 (2018).

3. Plasmonic-Enhanced Lab-on-a-Chip Device for Bacteria Drug Susceptibility (Under preparation).

3.1. Introduction:

Following the emergence of antibiotics that have transformed medicine and saved millions of lives, monitoring bacteria viability and antibiotics efficacy on resistant pathogenic bacteria can reduce the detrimental effects of pathogens on human lives.[1] Antibiotic-resistant strains of pathogenic bacteria can be generated as a result of misuse of antibiotics[1], and exposure to sub-therapeutic concentrations of antibiotics[1]. Thus, the development of a simple, rapid and sensitive approach for phenotypic profiling of drug resistivity and monitoring metabolic reactions is of importance.[2,3] A variety of methods has been developed to address this issue including bacteria culture tests,[4,5] real-time multiplex polymerase chain reaction (PCR),[6,7] matrix-assisted laser desorption/ionization time-of-flight mass spectrometry,[8] and colorimetric assays,[9] which typically give results after 48, 4, 6, and 28 hours, respectively. The colorimetric approach has been used clinically, illustrating many key advantages such as ease of operation, ability to emblement in low resource settings, and no need for expensive reagents. Despite all the advances in colorimetric indications, these approaches lack enough sensitivity and rapidity for point of need applications.

As an alternative method, microfluidic technology has been studied as a potential candidate for bacterial antibiotic resistance screening allowing for handling small fluid volumes (10^{-18} to 10^{-6} Liters).[10,11] Microfluidic devices with low sample/reagent consumption can lead in economic manufacturing costs.[12] Microfluidic platforms can screen for antibiotic resistance using various techniques including optical detection.[13] Fengjiao Lyu et al[14] used a droplet microfluidic platform for bacterial antibiotic resistance screening. They used a fluorescent readout system depending on a Resazurin (Alamar blue) assay. The platform separated the antibiotic and Alamar blue mixing steps for added process control. They were able to achieve a single-cell resolution to assess hetero-resistance in sample sub-populations, and they had an operating time of 3 hours. Azizi et al[15] proposed the use of a nanoliter-sized microchamber for rapid identification of

antibiotic resistance profiles. Like the previous group, they used a fluorescent readout system depending on a Resazurin (Alamar blue) assay. A readout time of 1-3 hours depending on the bacterial concentration was reported. Elavarasan et al[16] developed a microfluidic device for assessing bacterial antibiotic susceptibility using colorimetric resazurin assay. They evaluated antibiotic resistance traits using various clinical isolates of diarrhoeagenic strains of Escherichia coli, Shigella flexneri, Shigella boydii, and Shigella sonnei. Their platform was able to identify resistant strains and minimum inhibitory concentrations of the antibiotics in 6-7 hours. Lee et al[17] were able to estimate antibiotic resistance and minimum inhibitory concentration for *Enterococcus*. Their readout system depended on the colorimetric results of their assay. The microfluidic device can detect the minimum inhibitory concentration after 24-hour incubation. A promising avenue for accelerating the colorimetric devices processing time is using plasmonic meta-surfaces.

Non-pigment based colors such as thin films, diffractive structures, and plasmonic colors drew a huge interest in recent years.[18] The color-generation strategy of plasmonic color printing involves the patterning of various geometrical metallic nanostructures such as nanodisks, ellipses, nanocubes and multimers based on Plasmon-supported materials such as gold,[19] silver[20] and aluminum.[21] The geometrical nanostructures and materials are designed to resonate at a specific optical frequency leading to the production of different colors across the visible spectrum.[22,23] Although direct-write technologies such as e-beam lithography[24,25] and focused ion-beam lithography[26] allow for patterning resolution and placement accuracy required to achieve the specific resonant, they are time-consuming, expensive and do not allow complex 3D structures. Recently, fabless approaches such as sacrificial polymeric nanoparticle templates, controlled phase separation, mesoporous particles assembly, and colloidal particles self-assembly[27,28] have been found promising alternatives for large-area patterning. Unlike the organic-dye color filters, the plasmonic color filters offer advantages such as high color tunability, sensitive color changing based on medium permittivity and low color degradation rate.[23,24,29,30] Using plasmonic platforms to facilitate rapid detection of metabolic resazurin reduction is an interesting venue. Resazurin is a weakly fluorescent dye characterized by its dark blue color. Resazurin undergoes a reduction reaction to the highly fluorescent pink colored resorufin. In presence of live cells resazurin diffuses/gets transported into the cell, where it is reduced to resorufin as a result of different redox enzymes in the intracellular environment such

as NADH.[31] Subsequently, reduced resorufin diffuses back to the extracellular environment. Jian Lin et al [32] confirmed that this NADH controlled reduction reaction can only happen in intracellular conditions in viable cells, thus acting as a cell viability indicator. We anticipate by incorporating the non-pigment plasmonic color platforms with microfluidic devices to allow simultaneous sensitive and high throughput colorimetric monitoring of antibiotic efficacy.

Here, we propose a novel fabless optical approach based on the integration of plasmonic meta-surfaces with fluidic sample delivery to directly monitor the NADH-control conversion of a colorimetric cell viability assay. Our approach does not require expensive instrumentation, highly skilled operators or extended incubation periods. The plasmonic fluidic device does not require dedicated external fluid actuation facilities as syringe pumps or pressurized pneumatic lines. It allows high-throughput, highly parallel, rapid and quantitative measurements, making our device an excellent point of need approach for assessing drug resistance profiles and monitoring metabolic reactions.

3.2. Experimental Section:

3.2.1. Platform/device fabrication

A fabless nano-patterning approach was implemented for the fabrication of the plasmonic platforms. First, we use a generic approach to develop a colloidal self-assembly monolayer (SAM) of nanoparticles at the water/air interface. This is followed by transferring the resulted honey-comb patterns to the silicon (Si) substrate. Next, we deposited a thin layer of ZnO (60 nm thick) as a low dielectric constant back reflector. This layer exhibits low-toxicity and good biodegradability, thus offering a suitable candidate to be used in the handling of biological samples. Lastly, an ultrathin layer of Al (15 nm thick) with the ability to provide tunable localized surface plasmon resonance was deposited to introduce vital high-resolution plasmonic color with a white background. The plasmonic platform can be integrated with a pre-patterned lab-on-chip device. The SAM layer can be selectively deposited on the fluidic chip to create a designated ultra-sensitive color-reading chamber.

The fluidic chip includes a bacteria trapping chamber (1.76 mm × 1.5 mm × 15 μm), color-reading chamber (1.97 mm × 1.5 mm × 15 μm), and inlet/outlet ports. The device layout was designed using AutoCAD® (Autodesk Inc., CA, USA). The microfluidic features were patterned

by an EVG620 mask aligner in a SU-8 layer (SU-8 2015, MicroChem Corp., MA, USA) on a 6 in. Silicon wafer, using a flexible photomask with the device design. Subsequently, the 6 in wafer was diced and individual chips were bonded to polydimethylsiloxane (PDMS SYLGARD 184 silicone elastomer, Dow Consumer Solutions, QC, Canada) to make a working device using established protocols.[33] Briefly, PDMS was mixed with curing agent at ratio 1:10 by weight and spin-coated on a dummy wafer. Next, a slap of cured PDMS was brought in contact with the liquid PDMS then put in contact with the microfluidic chip and left to dry for 48 hours.

3.2.2. Bacteria Culture.

Ampicillin resistant Escherichia coli strain (Amp resistant *E. coli*, # 211540, Merlan scientific, Ontario, Canada) was cultured overnight at 37℃ in Luria broth (LB) media supplemented with 100µg/mL Ampicillin (# 216858, Merlan scientific, Ontario, Canada). Next, the bacterial concentration was determined by optical density technique using a Spectronic 21D spectrophotometer. Subsequently, aliquots of different concentrations were prepared for the antibiotic susceptibility testing experiments.

3.2.3. Antibiotic susceptibility screening.

For resistant bacterial samples, we prepared aliquots of Amp resistant *E. coli* with different concentrations (10^{05} Cells/mL, 10^{03} $\frac{cells}{mL}$,10^{02} Cells/mL, and 50 Cells/mL) using a resazurin/ampicillin solution of 1mM resazurin (R7017, Millipore Sigma, Ontario, Canada) + 100 µg/mL Ampicillin concentration. The aliquots were incubated at 37℃ different time periods starting from 0 minutes incubation till 60 minutes with a time step of 5 minutes. For susceptible bacterial samples we prepared aliquots of Amp resistant *E. coli* with different concentrations (10^{05} Cells/mL, 10^{03} $\frac{cells}{mL}$,10^{02} Cells/mL, and 50 Cells/mL) using a resazurin/kanamycin solution of 1 mM resazurin + 50 µg/mL kanamycin (# 216862, Merlan scientific, Ontario, Canada) concentration. The aliquots were incubated at 37℃ different time periods starting from 0 minutes incubation till 60 minutes with a time step of 5 minutes.

For minimum inhibitory concentration (MIC) study, we used aliquots of 5×10^{5} Cells/mL Amp resistant *E. coli* with resazurin/kanamycin solution. We used solutions with different kanamycin concentrations of 1 µg/mL, 2 µg/mL, 4 µg/mL, 8 µg/mL, 16 µg/mL, 32 µg/mL, and 50 µg/mL to

determine the MIC dose.

For the Clinical & Laboratory Standards Institute (CLSI) MIC protocol E coli bacteria were streaked on LB agar overnight and resuspended in water aliquot. The aliquot was measured, and the bacteria concentration was adjusted to 10^{06} CFU/mL in LB media. A 96 well plate with an antibiotic gradient from 128 μg/ml to 0.125 μg/ml in a 2-fold concentration dilution step was prepared with a positive control with no antibiotics. Next, the bacteria were introduced to each well of the 96 well plate for a final bacteria concentration of 5×10^{05} CFU/mL. The well plates were cultured overnight the minimum inhibitory concentration was determined as the antibiotic concentration that didn't show any signs of bacterial growth.

To rapidly detect the sample color change on the platform we measured the reflectance spectra using a Lambda 750 UV/Vis/NIR Spectrophotometer (PerkinElmer). The incident and collected light beams had normal incidence to the platform. Also, we performed optical imaging under highly controlled environment using Nikon Eclipse LV150 (Nikon) with a ×100, 0.9 NA air objective and Nikon digital sight ds-fi1 CCD camera with a white reference of R:0.75 G:1.0 B:2.36.[34]

3.2.4. Image processing and analysis.

All images were processed and analyzed through a MATLAB script which allows the analysis of multiple images simultaneously. The TIFF files were loaded and cropped to 80% of its original dimensions to avoid the coffee-ring effect.[35] An option for the manual crop was also available. For each image, five samples of 480 x 480 pixels were randomly selected. Subsequently, for each the R, G and B values were averaged followed by the calculation of the mean RGB value and error across them. Succeeding their conversion to *XYZ* and *x, y* color systems. The RGB values of each image with its corresponding error bar were plotted against time. Additionally, the *x* and *y* values were scattered on the CIE1931 color space to analyze the color change through time.

3.3. Results:

The integrated plasmonic device operates based on two chambers 1) plasmonic color-sensitive chamber and 2) antibiotic infusing chamber equipped with bacteria entrapping micropillars. The functionality of the plasmonic device is attributed to the unique characteristics of the plasmonic

nano-surface in terms of detecting the color change according to the changes in the media. Figure 3.1 shows the schematic illustration of the device. The device consists of different compartments including the plasmonic color-sensitive chamber, the mixing and entrapment chamber, the inlet and outlet ports. The operational procedure of the device is to inject the bacteria containing media along with antibiotic of interest and resazurin from the inlet to get mixed in the mixing and entrapment chamber. Devices will be incubated for one hour through time intervals of 5 minutes. After incubation, the liquid in the trapping chamber will be pushed towards the plasmonic color-sensitive chamber while the bacteria will be entrapped behind the micropillars.[36]

The plasmonic color-sensitive platform is fabricated via a self-assembly monolayer method using polystyrene nanoparticles with a variety of sizes (d=200-1000 nm). The hexagonal close-packed (HCP) lattice of the nanoparticles (Figure 3.1d) was used to fabricate the plasmonic substrate by deposition of back-reflector (ZnO) and a thin film of Al. The ZnO back-reflector allows for reducing the toxicity of the color-sensitive chamber to minimize the risk of manipulating antibiotic effect by the platform.[37]

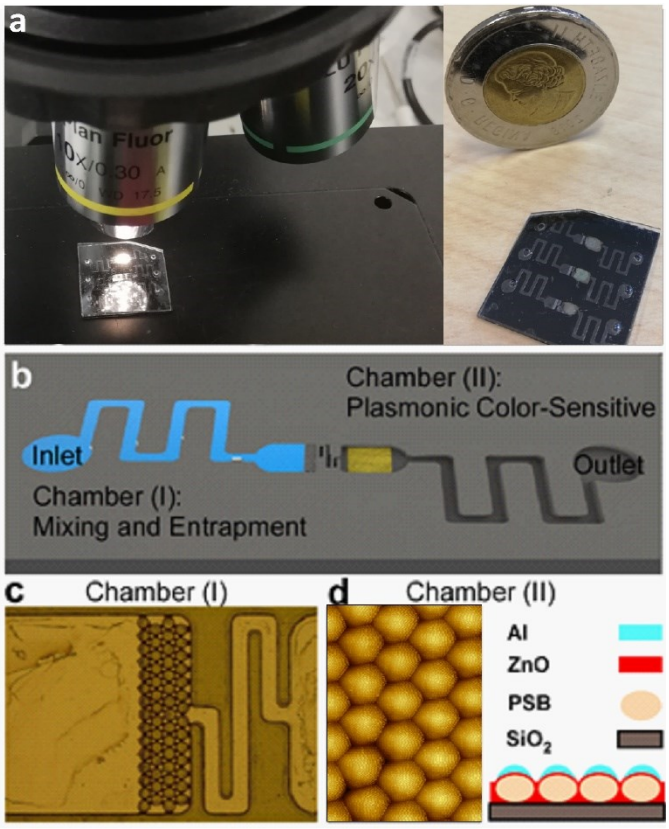

Figure 3. 1 Microfluidic device for the assessment of bacterial susceptibility to antibiotics.

A) Microscopy setup to capture colours of the microfluidic chamber with high fidelity colours. Inset, a fabricated plasmonic-enhanced Lab-on-a-Chip device with a coin for size reference. B) A zoom of the highlighted area in a is presented. The device design of a single channel with two ports (inlet and outlet) and two chambers. C) Chamber I is designed for the mixing and entrapment of the solution infused as it encounters the pillar array. D) In Chamber II, the color is sensed through the plasmonic properties of the surface. A cross-section is presented, the resonances are given by the following arrangement: nanoparticles SAM, coated by a ZnO layer and a thin Al deposition.

The resazurin reduction assay was widely used as a viability reagent in drug screening studies.[38] Viable bacteria (cells) turn resazurin to resorufin via their NADH-control metabolism which in turn change the color of the media from navy blue (resazurin) to light pink (resorufin). Unlike the vast usage of this method, few attempts have been done to enhance the sensitivity, rapidity, and quantifiability of the results. Here, we propose to utilize a fabless plasmonic color platform to support the demonstration of broad color change during the NADH-control conversion of resazurin to resorufin in more sensitive detail, as an indicator for cell viability in presence of different chemicals. Unlike the organic-dye color filters, the plasmonic color filters offer advantages such as high color tunability, sensitive color changing based on medium permittivity and low color degradation rate.[23,24,29,30]

The color sensitivity of the plasmonic platform against the diameter of the nanoparticle is demonstrated in Figure 3.2. The color of the plasmonic platform depends on geometrical features of the plasmonic nanostructures i.e. size and pitch of nanoparticles as well as the refractive index of the surrounding medium.[39] In a close-packed lattice of the self-assembled nanoparticles, the diameter of the nanoparticles also determines the pitch of the lattice.[21] Plasmonic color-sensitive platforms with diameters from 200 nm to 1000 nm were investigated and compared with conventional glass substrate in different media; air, water, LB, resazurin, and resorufin (Figure 3.2a). In each media, the same self-assembled plasmonic substrate was used to eliminate the shape factors, structural defects, and other matrix effects. To investigate the color gamut throughout the conversion of resazurin to resorufin, RGB values were extracted from the microscopy images and converted to x-y coordinates on standard CIE 1931 chromaticity diagram (figure 3.2b). The lattice made by 400 nm nanoparticles demonstrates a larger color gamut between resazurin (navy-blue) to resorufin (cyan-green).

The absorption efficiency of the plasmonic nanoparticles in each medium with a specific refractive index determines the vitality of the generated color. The energy of the beam incident is removed from the beam path upon its interaction with plasmonic matter by absorption and

scattering.[40]

The conventional metric to study the superiority of the structure is the absorption efficiency which is the ratio of the absorption cross-section to the geometric cross-section. The absorption efficiency for a cylindrical particle illuminated along its axis is given by:[41]

$$\boldsymbol{Q_{abs}} = \frac{4\sigma_{abs}}{\pi d^2} \tag{3.7}$$

where d is the diameter of the nanoparticle and σ_{abs} is the absorption cross-section which can be calculated with dividing the power absorbed by nanoparticle over the incident irradiance.

Figures 3.2c to 3.2e demonstrates the experimental reflectance spectra for the 400 nm, 600 nm and 750 nm plasmonic platform performed in water-based media. The origin of the different resonances can be attributed to the two-fold role of the plasmonic structures. Wong et al. observed a similar strong plasmon coupling behavior in a self-assembled nanoparticle platform for color-printing in air.[42] Local resonances are responsible for color shifts. Localized surface plasmon resonance (LSPR) given by dipolar coupling between adjacent structures and surface plasmon resonance (SPR) from the structured array gives rise to hot-spots regions located by the space given by the cavity length and space in between structures, also known as nanocavity. In our system, the periodic bumps formed by nanoparticles act as coupling elements to excite propagating surface plasmons (SPs) on the surface. Since the Al layer is ultrathin, these SPs couples to the top metallic-liquid interface. The light re-radiated from those coupled plasmons interferes with the directly reflected light and generates resonance dips in the reflection spectrum. At shorter wavelengths, a sharp reflectance dip is expected to translate the lattice resonance.[21,43] Opposite, at longer wavelengths the dips attributed to high-order mode are expected to be broader.[44] For color-sensitive sensing application described herein, we chose the second spectral feature (dip) that showed the best sensitivity towards the changes in the refractive index of the liquid media. The high order mode dip exhibits a blue shift along with the reduction of resazurin to resorufin. Figure 3.2f to 3.2h demonstrates the corresponding changes in the aforementioned dips (ΔDip). Moreover, the high order mode is blue-shifted by~10 nm from 400 nm platform to 600 nm platform. Semi dips are also observed across all measurements in 600 nm and 750 nm platforms at visible frequencies, the penetration depth of the propagating

SP modes into a surrounding dielectric media can vary between 100-300 nm. The penetrated propagating SP modes are subjected to alter by changing the refractive index (RI) of the medium. The additional informetric dip correlated to resazurin media is demonstrated by dotted line. According to the comparison between the blue shifts occurred in the second dip positions (red) for 400 nm substrate is higher (37 nm) compared to other substrates. Thus, it is elicited that 400 nm substrate is most effective among others in terms of spectral sensitivity during reduction of resazurin to resorufin which is in agreement with the analysis of the bright-field micrographs.

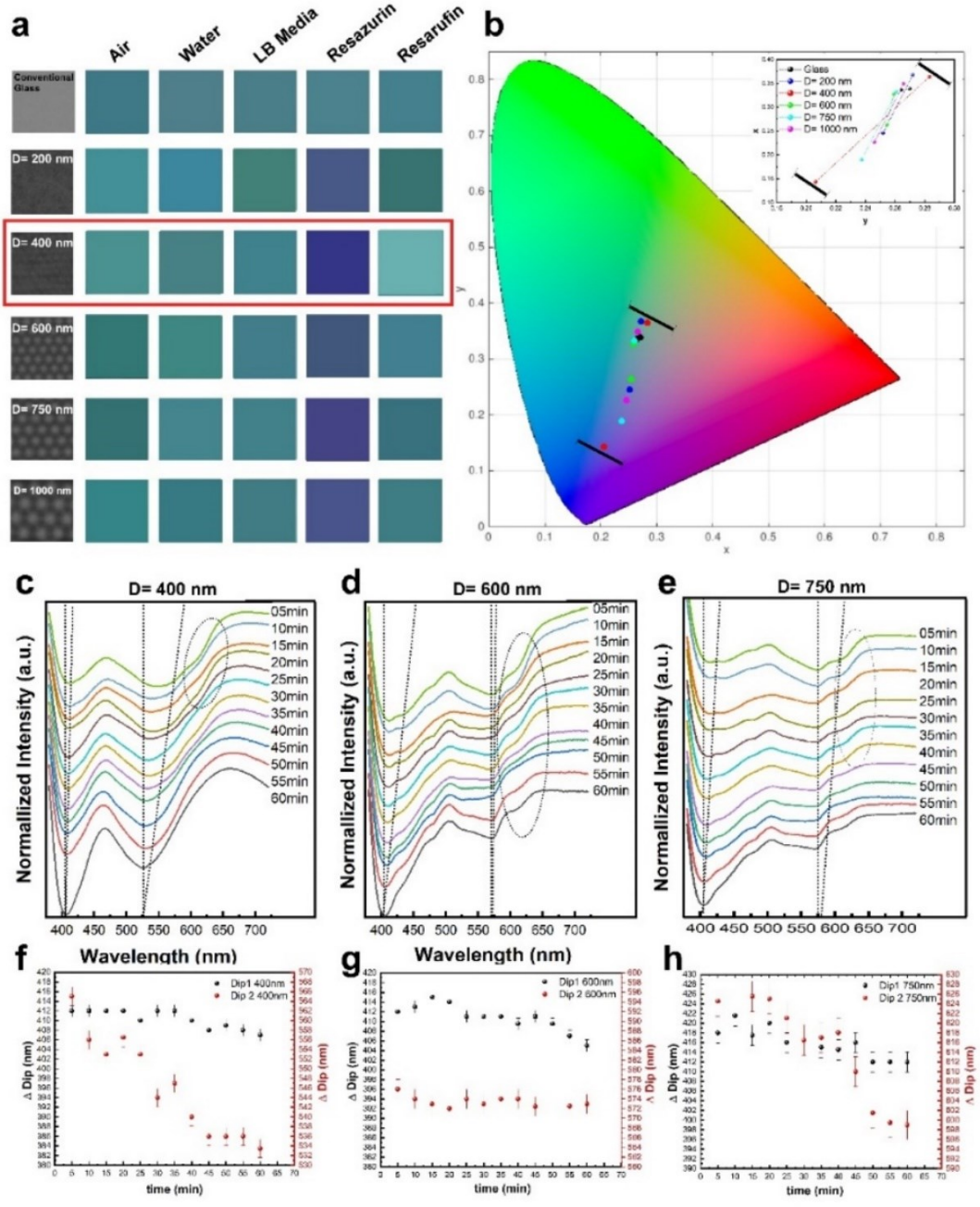

Figure 3. 2 Platform optimization study.

a) Bright-field microscopy of different platforms (glass, 200 nm, 400 nm, 600 nm, 750 nm, and 1000 nm nanoparticles diameter) under D50 white light. Different media were used including air, water, LB media (RI. 1.338), resazurin, and resorufin. The widest gamut change was observed in the 400nm platform. b) 2D CIE 1931 chromaticity diagram showing the color change between the resazurin and resorufin for different platforms. c-e) Reflectance spectra of 400 nm, 600 nm and 750 nm platforms during resazurin reduction to resorufin respectively. f-h) Dip position for 400 nm, 600 nm, and 750 nm platforms during resazurin reduction to resorufin respectively.

To investigate the sensitivity and rapidity of the color-sensitive plasmonic platform in antibiotic efficacy, a thorough study has been performed via bright-field microscopy. Knowing that the resistant bacteria strains to an antibiotic are expected to cause a reduction of resazurin to resorufin which in turn results in a color change from navy-blue to green the antibiotic susceptibility profile of Ampicillin resistant *E. coli* bacteria was evaluated using the 400 nm plasmonic platforms.

Figure 3.3 demonstrates the sensitivity of the platform towards the metabolic reaction of the Ampicillin-resistant strain of *E. coli* in the presence of Ampicillin (3.3a) and Kanamycin (3.3c) at different initial concentrations of bacteria during 5-minutes intervals of incubation with the antibiotic. As expected, the liquid containing Ampicillin-resistant *E. coli* and concentrated Ampicillin (100 μg/ml) shows the full gamut from blue to green (Figure 3.3b) over incubation for an hour while presence of concentrated Kanamycin (50 μg/ml) hindered the change in the color. Figure 3.3a demonstrates that although the rapidity of the detection decreases by lowering the initial concentration of bacteria, the plasmonic platform is able to identify the efficacy of antibiotics on the bacterial strain under 60 minutes. For the 10^5 CFU/mL after 30 minutes incubation a dark cyan color is observed as a result of resazurin reduction to resorufin indicating the resistant profile of the *E.coli* versus ampicillin. This is a significant advancement to the previously reported time in the literature 4 hours for 10^5 CFU/ml bacteria concentration.[45,46] For 10^3 CFU/mL *E.coli* concentration after 45 minutes incubation dark cyan color can be observed signaling their resistant traits. Color change to dark cyan can be observed after 55-minute incubation for 10^2 CFU/mL *E.coli*. Figure 3.3b plots the trend of color change on CIE chromaticity diagrams for different *E. coli* concentrations. For 10^5 CFU/mL concentration gradual color change from navy blue for 0 minutes incubation to green for 60minutes incubation is observed. Lower concentrations exhibit the same color change trend with decreased rapidity. This is due to the slower reduction rate of resazurin in presence of lower bacterial

concentrations.[47,48] In contrast, No color change was observed when the *E. coli* were in the presence of concentrated Kanamycin. This is due to the absence of resazurin reduction by viable bacteria and thus indicates the susceptibility of *E.coli* to kanamycin. This is further demonstrated in the CIE chromaticity diagrams (Figure 3.3d) confirming that the color remained in the region of navy blue/ dark purple which indicates the absence of metabolic reactions in the aliquots.

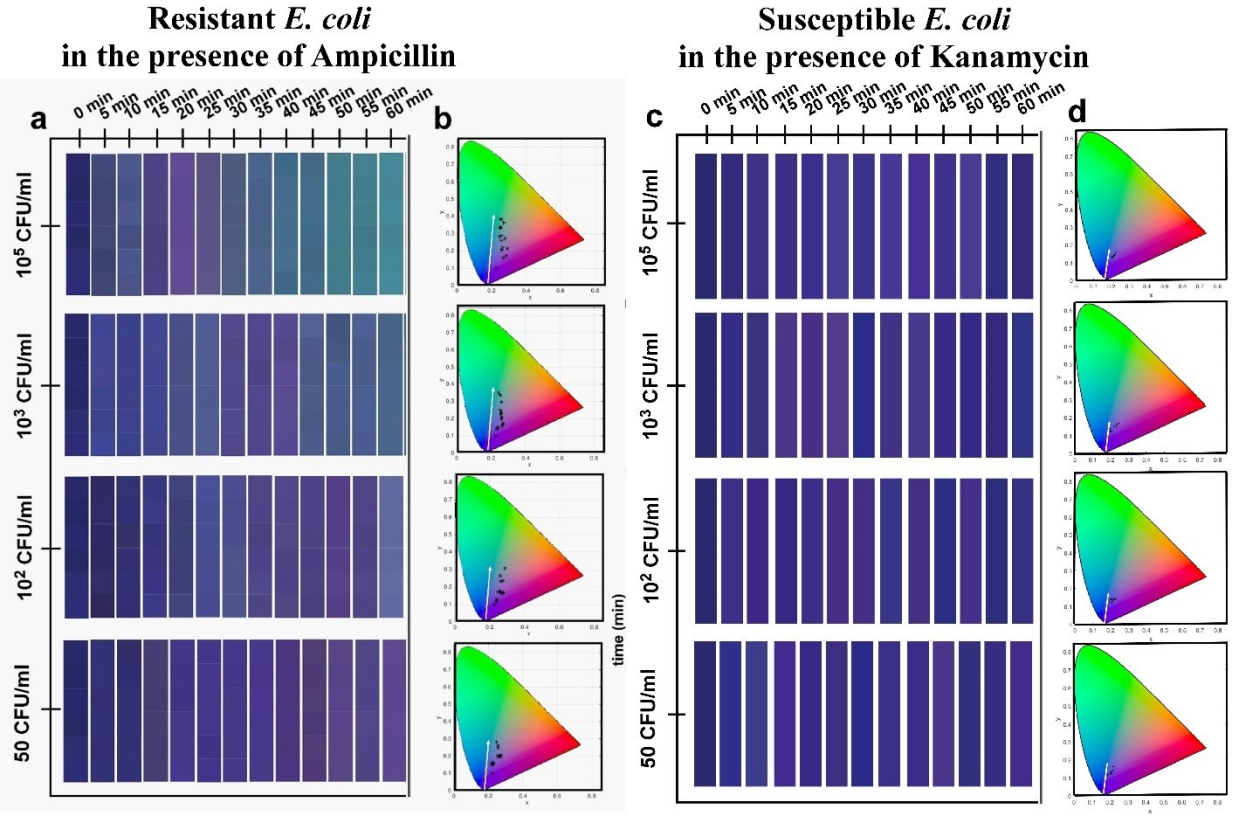

Figure 3. 3 E.coli antibiotic susceptibility study.

a) Color response of 400 nm platform using aliquots of different concentrations of Amp resistant E. coli mixed with resazurin and ampicillin. The aliquots were incubated at 37 Celsius for different durations from 0 minutes to 60 minutes. b) 2D CIE chromaticity diagram showing the color change due to resazurin reduction to resorufin during 60 min incubation for different E. coli concentrations 10^5, 10^3, 10^2 and 50 CFU/mL (figures b-I to b-IV respectively). c) Color response of 400nm platform using aliquots of different concentrations of Amp resistant E. coli mixed with resazurin and kanamycin. The aliquots were incubated at 37 Celsius for different durations from 0 minutes to 60 minutes. d) 2D CIE chromaticity diagram showing the color response of the 400 nm platform for different E. coli concentrations 10^5, 10^3, 10^2 and 50 CFU/mL (figures d-I to d-IV respectively).

The color change gamut demonstrated in Figure 3.3 correlating to the metabolic reaction of resistant bacteria was further analyzed in Figure 3.4. The Tristimulus values of the XYZ color space were calculated from the bright-field microscopy images and used to assess the color change. Figure 3.4a demonstrates the change of Y values versus incubation time for different *E.*

coli concentrations, respectively. All concentrations of *E. coli* exhibit a general increase in the Y value over 60 minutes of incubation in the presence of resazurin: 10^5 CFU/mL (ΔY= 90,000), 10^3 CFU/mL (ΔY= 90,000) , 10^2 CFU/mL (ΔY= 65000), and 50 CFU/mL (ΔY=60000). The increase in Y coordinate indicates changing to a more luminous (brighter) color. Also, noting that y coordinate of the chromaticity diagram is the normalized form of the Y coordinate ($y = \frac{Y}{X+Y+Z}$). Accordingly, an increase in Y value is directly correlated to color change towards the green/cyan region of the chromaticity diagram. The distribution of Y-value (Figure 3.4b) demonstrates that higher bacterial concentrations exhibited faster color change. For zero-minute incubation, all exhibited a navy blue/ dark purple color. The first change of color was observed at 5 minutes, 20 minutes and 40 minutes for 10^5 CFU/mL and 10^3 CFU/mL, 10^2 CFU/mL and 50 CFU/mL, respectively. The second color transition was observed at 20 minutes, 30 minutes, 40 minutes and 60 minutes for E. coli concentrations of 10^5 CFU/mL, 10^3 CFU/mL, 10^2 CFU/mL, and 50 CFU/mL, respectively. The color change towards green occurred after 40 minutes and 60 minutes, of incubation for *E. coli* concentrations of 10^5 CFU/mL and 10^3 CFU/mL, respectively (Figure 3.4c).

Figure 3.4d shows the reflectance spectra of the 400 nm platform in the presence of different concentrations of resistant *E.coli* bacteria. As expected, the higher *E. coli* concentrations exhibit a more pronounced blue shift blue shift in the second dip, corresponded to the high order resonance. The 10^5 CFU/mL concentration of resistant bacteria exhibited a total blue shift of 35 nm while the 10^3 CFU/mL exhibited 20nm blue shift in dip position (Figure 3.4e). The dip shift decreases with lower initial bacterial concentrations during the 60 minutes incubation.

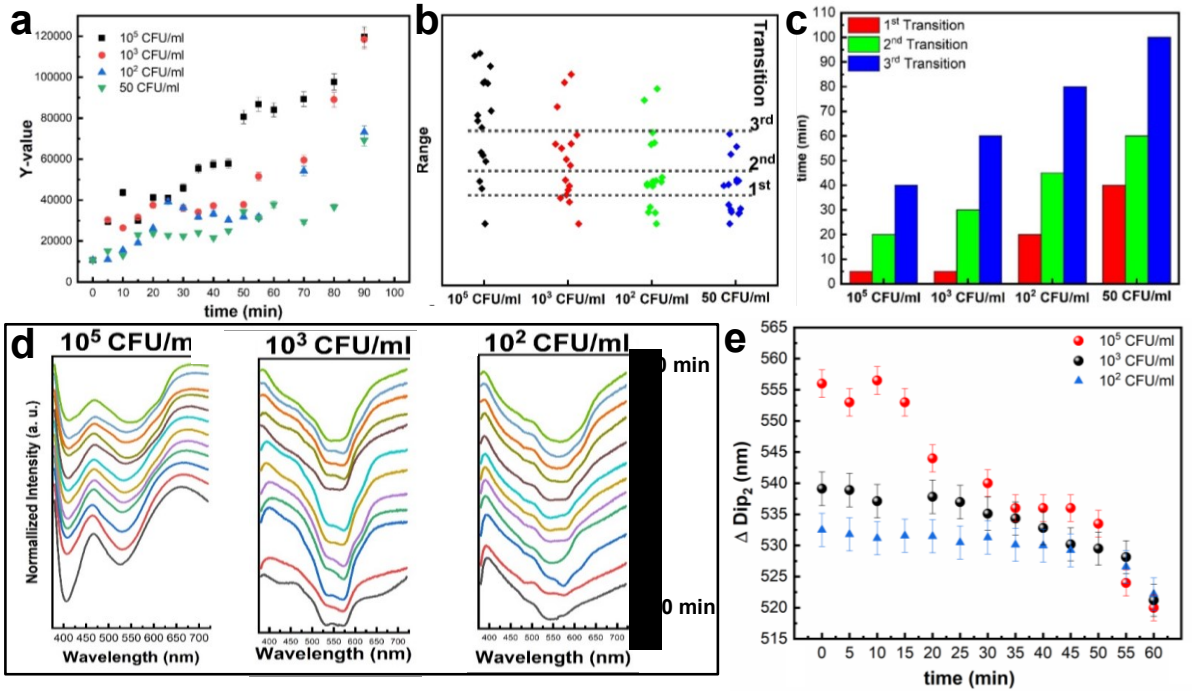

Figure 3. 4 Colorimetric analysis of platform sensitivity.

a) Y-value extracted from RGB values of random-picked micrographs. (b) Distribution of y-value representing averaged RGB-value of 5 points in the microscopy. (c) Concentration sensitivity of the platform with respect to its response time. (d) Reflectance spectra of 400 nm platform during Resazurin reduction to Resorufin for different bacterial concentrations. e) Second dip position during resazurin to resorufin reduction for 10^5 CFU/mL (red) and 10^3 CFU/ml (black) and 10^2 CFU/mL (blue).

A minimum inhibitory concentration (MIC) study for *E. coli* was conducted to determine the minimum Kanamycin dose that would prevent further bacterial growth and proliferation. It is expected that the Kanamycin MIC would show no color change while lower concentration would exhibit a color change trend indicative of resazurin reduction by viable bacteria. 5×10^5 CFU/mL *E. coli* aliquots were challenged with different concentrations of kanamycin. The aliquots were incubated at 37℃ for different time durations ranging from 0 minutes to 60 minutes with 5 minutes time intervals. Figure 3.5 demonstrates the MIC evaluation using the 400 nm plasmonic platform in under 60 minutes. Figure 3.5a shows that upon 60 minutes incubation, the Ampicillin-resistant E. coli displayed color change from navy blue towards cyan depending on the concentration of Kanamycin (1 µg/mL, 2 µg/mL, and 4 µg/mL). The corresponding color gamut is illustrated in the CIE diagram (Figure 3.5b). The concentrations of Kanamycin with which the bacteria were susceptible and resistant are marked with S and R, respectively. For 1 µg/mL Kanamycin a clear color change was observed after 35 minutes of incubation which is in

agreement with previous experiments on resistive bacteria (Figure 3.5c). The corresponding trend of color change is demonstrated on the CIE diagram (Figure 3.5d) 8 µg/mL and 50 µg/mL kanamycin concentrations show a consistent navy blue/ dark purple color throughout the entire incubation period of one hour suggesting of the susceptibility of bacteria. In contrast, the lower concentrations of Kanamycin led bacteria to continue with NADH-control changing the color, suggesting the bacteria remained resistant. Thus, we determined the minimum inhibitory concentration of Kanamycin for the *E. coli* bacteria to be 8 µg/mL. Thus, it is concluded that the *E. coli* aliquots are susceptible to Kanamycin according to the Clinical & Laboratory Standards Institute -CLSI- criteria (Susceptible ≤ 16; Resistant ≥ 64 mg/L).[49] This is in close agreement (within an acceptable variation of two-fold dilution according to CLSI standards) with the standard CLSI MIC test we did and earlier studies.[50]

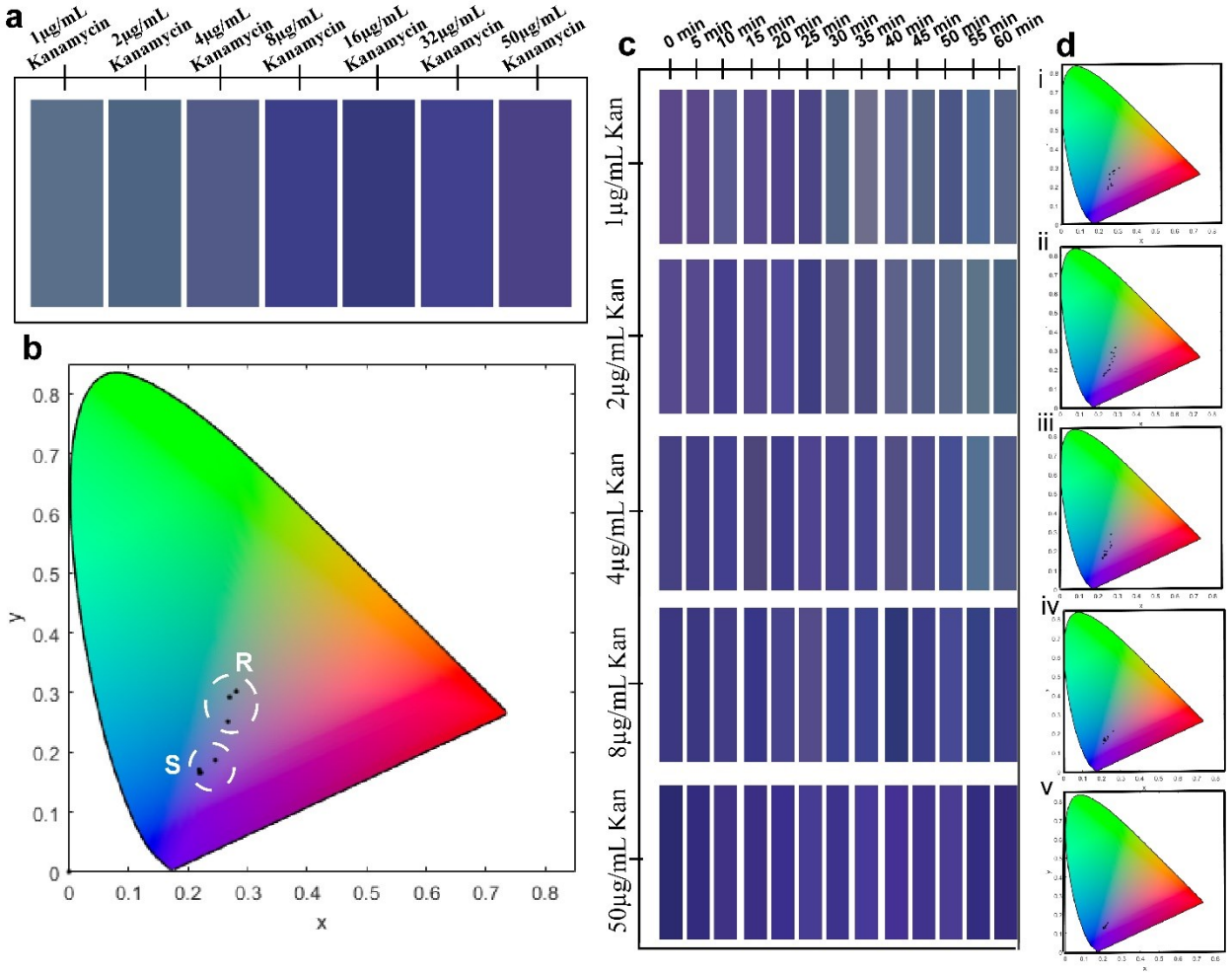

Figure 3. 5 Determination of MIC for Kanamycin against Amp. Resistant E.coli.

a) Color response of 400nm plasmonic platform using aliquots of 5×10^5 CFU/mL Amp resistant E. coli incubated at 37 ℃ for 60 minutes with resazurin and different concentrations of Kanamycin (1 μg/mL, 2 μg/mL, 4 μg/mL, 8 μg/mL, 16 μg/mL, 32 μg/mL, and 50 μg/mL). The 1μg/mL, 2 μg/mL, and 4 μg/mL, Kanamycin doses were not enough to fully inhibit the E. coli metabolism as shown by the color change witnessed from purple to cyan. b) 2D CIE chromaticity diagram showing the color change due to resazurin reduction by living E. coli bacteria. Aliquots treated with low doses of kanamycin (1 μg/mL, 2 μg/mL, and 4 μg/mL) exhibited a color shift towards cyan and were labeled with R as resistant bacteria. Alternatively, aliquots treated with higher doses of Kanamycin (8 μg/mL, 16 μg/mL, 32 μg/mL, and 50μg/mL) didn't show color change and were labeled as S as susceptible bacteria. c) Platform color response for aliquots incubated for different time durations from 0 minutes to 60 minutes. d) 2D CIE chromaticity diagram showing the color change trend due to resazurin reduction to resorufin during 60 min incubation for 5×10^5 CFU/mL E. coli versus 1 μg/mL, 2 μg/mL, 4 μg/mL, 8 μg/mL, and 50 μg/mL doses of Kanamycin (figures b-I to b-v respectively).

In order to more conveniently convert the microscopy results to the feasible CIE color gamut, each picture of the data set loaded to MATLAB was read as a 3 layers matrix, each pixel has 3 components, one per layer, corresponding to its R, G and B value. The processing involved image crop and a sample selection (see Experimental section). A simple average calculation was run individually to get an overall value for R, G and B components for each of the 5 samples generated. After, the mean across the collection was calculated. The error bar was computed at 1 standard deviation.

The conversion to XYZ color systems was made through a software function, using as white point reference the CIE standard illuminant pair: D50, [0.9642, 1.0000, 0.8251] also known as 'horizon light' which is correlated color temperature of 5003 K.

The x and y values were calculated following the equations (3.2 and 3.3) afterward they were used as coordinates to ubicate the overall color value of each picture in the data set into the International Commission on Illumination color space widely known as CIE 1931 to evaluate the total spanning of the resazurin color change.[51]

$$x = \frac{X}{X + Y + Z} \tag{3.2}$$

$$y = \frac{Y}{X + Y + Z} \tag{3.3}$$

3.4. Conclusion

Here we presented plasmonic enhanced integrated microfluidic device for colorimetric antibiotic susceptibility screening. The device incorporates a bacteria capture chamber, a filter

element based on pillar PSP interaction for bacteria trapping and color reading chamber for antibiotic susceptibility profiling. For rapid colorimetric readout a plasmonic platform was developed. It incorporated self-assembled monolayer of nano-particles deposited with Zinc Oxide spacer layer and an Aluminum layer. We evaluated the effect of using different sized nanoparticles of the color reading performance of the plasmonic platform. Bright-field microscopy images and UV-vis measured reflectance spectra for different platforms were compared. The plasmonic platform with 400 nm diameter nanoparticles exhibited the widest color gamut and thus presented the optimum platform for sensitive detection of color change. The antibiotic susceptibility profile for different concentrations of ampicillin-resistant *E coli* strain was evaluated against ampicillin and kanamycin. The ampicillin resistance was identified in 30 minutes for E coli concentration of 10^{05} CFU/mL. Where for the 100 CFU/mL E coli concentration the resazurin reduction was identified after 60 minutes. Also, the MIC for Kanamycin against the *E coli* strain was measured to 8 μg/mL using the plasmonic platform. The MIC of Kanamycin was confirmed to be 4 μg/mL using the standard procedure outlined by CLSI. Thus, the result of the device is within acceptable 2-fold concentration variation from the CLSI protocol. Last, a MATLAB code was developed for automated analysis of the obtained microscopy imaging.

3.5. References**:**

1. Ventola, C. L. The antibiotic resistance crisis: part 1: causes and threats. *Pharm. Ther. J.* **40**, 277–83 (2015).

2. Spellberg, B. & Gilbert, D. N. The future of antibiotics and resistance: a tribute to a career of leadership by John Bartlett. *Clin. Infect. Dis.* **59 Suppl 2**, S71–S75 (2014).

3. Ventola, C. L. The antibiotic resistance crisis: part 2: management strategies and new agents. *P T* **40**, 344–352 (2015).

4. Organization, W. H. *Manual for the laboratory identification and antimicrobial susceptibility testing of bacterial pathogens of public health importance in the developing world: Haemophilus influenzae, Neisseria meningitidis, Streptococcus pneumoniae, Neisseria gonorrhoea, S.* (Geneva: World Health Organization, 2003).

5. *CLSI. Methods for Dilution Antimicrobial Susceptibility Tests f or Bacteria That Grow Aerobically; Approved St andard—Ninth Edition.* (2012).

6. Maxson, T., Blancett, C. D., Graham, A. S., Stefan, C. P. & Minogue, T. D. Rapid antibiotic susceptibility testing from blood culture bottles with species agnostic real-time polymerase chain reaction. *PLoS One* **13**, e0209042–e0209042 (2018).

7. Whiley, D. M. *et al.* Molecular Antimicrobial Resistance Surveillance for Neisseria gonorrhoeae, Northern Territory, Australia. *Emerg. Infect. Dis.* **23**, 1478–1485 (2017).

8. Vatanshenassan, M. *et al.* Proof of Concept for MBT ASTRA, a Rapid Matrix-Assisted Laser Desorption Ionization–Time of Flight Mass Spectrometry (MALDI-TOF MS)-Based Method To Detect Caspofungin Resistance in <span class="named-content genus-species" id="named-cont. *J. Clin. Microbiol.* **56**, e00420-18 (2018).

9. Elshikh, M. *et al.* Resazurin-based 96-well plate microdilution method for the determination of minimum inhibitory concentration of biosurfactants. *Biotechnol. Lett.* **38**, 1015–1019 (2016).

10. Sun, H. *et al.* Reliable and reusable whole polypropylene plastic microfluidic devices for a rapid, low-cost antimicrobial susceptibility test. *Lab Chip* **19**, 2915–2924 (2019).

11. Manz, A. *et al.* Planar chips technology for miniaturization and integration of separation techniques into monitoring systems: Capillary electrophoresis on a chip. *J. Chromatogr. A* **593**, 253–258 (1992).

12. Maguire, I., O'Kennedy, R., Ducrée, J. & Regan, F. A review of centrifugal microfluidics in environmental monitoring. *Anal. Methods* **10**, 1497–1515 (2018).

13. Kelley, S. O. New Technologies for Rapid Bacterial Identification and Antibiotic Resistance Profiling. *SLAS Technol.* **22**, 113–121 (2017).

14. Lyu, F. *et al.* Phenotyping antibiotic resistance with single-cell resolution for the detection of heteroresistance. *Sensors Actuators, B Chem.* **270**, 396–404 (2018).

15. Abbaspourrad, A. *et al.* Nanoliter-Sized Microchamber/Microarray Microfluidic Platform for Antibiotic Susceptibility Testing. *Anal. Chem.* **90**, 14137–14144 (2018).

16. Elavarasan, T., Chhina, S. K., Parameswaran (Ash), M. & Sankaran, K. Resazurin reduction based colorimetric antibiogram in microfluidic plastic chip. *Sensors Actuators B Chem.* **176**, 174–180 (2013).

17. Lee, W.-B. *et al.* A microfluidic device for antimicrobial susceptibility testing based on a broth dilution method. *Biosens. Bioelectron.* **87**, 669–678 (2017).

18. Jalali, M. *et al.* Stacking of colors in exfoliable plasmonic superlattices. *Nanoscale* **8**, 18228–18234 (2016).

19. Dreaden, E. C., Alkilany, A. M., Huang, X., Murphy, C. J. & El-Sayed, M. A. The golden age: Gold nanoparticles for biomedicine. *Chem. Soc. Rev.* **41**, 2740–2779 (2012).

20. Si, G. *et al.* Reflective plasmonic color filters based on lithographically patterned silver nanorod arrays. *Nanoscale* **5**, 6243–6248 (2013).

21. Wang, L. *et al.* Large Area Plasmonic Color Palettes with Expanded Gamut Using Colloidal Self-Assembly. *ACS Photonics* **3**, 627–633 (2016).

22. Halas, N. J., Lal, S., Chang, W. S., Link, S. & Nordlander, P. Plasmons in strongly coupled metallic nanostructures. *Chem. Rev.* **111**, 3913–3961 (2011).

23. Gu, Y., Zhang, L., Yang, J. K. W., Yeo, S. P. & Qiu, C. W. Color generation via subwavelength plasmonic nanostructures. *Nanoscale* **7**, 6409–6419 (2015).

24. Kumar, K. *et al.* Printing colour at the optical diffraction limit. *Nat. Nanotechnol.* **7**, 557–561 (2012).

25. Duan, H., Hu, H., Kumar, K., Shen, Z. & Yang, J. K. W. Direct and reliable patterning of plasmonic nanostructures with sub-10-nm gaps. *ACS Nano* **5**, 7593–7600 (2011).

26. F. Watt, A.A. Betiol, J.A. Van Kan, E. J. T. and M. B. . B. ION BEAM LITHOGRAPHY AND NANOFABRICATION : Next generation lithographies (NGLs) are being actively developed to take over from the highly successful optical lithography . As feature sizes shrink well below 100 nm , several key challenges for optical lit. *Int. J. Nanosci.* **4**, 269–286 (2005).

27. Innocenzi, P. *et al.* Hierarchical Mesoporous Films : From Self-Assembly to Porosity with Different Length Scales. 2501–2509 (2011). doi:10.1021/cm200050r

28. Zhang, B. J., Li, Y., Zhang, X. & Yang, B. Colloidal Self-Assembly Meets Nanofabrication : From Two- Dimensional Colloidal Crystals to Nanostructure Arrays. **130012**, 4249–4269 (2010).

29. Yokogawa, S., Burgos, S. P. & Atwater, H. A. Plasmonic color filters for CMOS image sensor applications. *Nano Lett.* **12**, 4349–4354 (2012).

30. Goh, X. M. *et al.* Three-dimensional plasmonic stereoscopic prints in full colour. *Nat.*

Commun. **5**, 1–8 (2015).

31. Riss, T. L. & Moravec, R. A. Chapter 4 - Cell Proliferation Assays: Improved Homogeneous Methods Used to Measure the Number of Cells in Culture. in (ed. Celis, J. E. B. T.-C. B. (Third E.) 25–31 (Academic Press, 2006). doi:https://doi.org/10.1016/B978-012164730-8/50005-8

32. Chen, J. L., Steele, T. W. J. & Stuckey, D. C. Metabolic reduction of resazurin; location within the cell for cytotoxicity assays. *Biotechnol. Bioeng.* **115**, 351–358 (2018).

33. Gajasinghe, R. W. R. L. *et al.* Experimental study of PDMS bonding to various substrates for monolithic microfluidic applications. *J. Micromechanics Microengineering* **24**, 75010 (2014).

34. Jalali, M. *et al.* A Hierarchical 3D Nanostructured Microfluidic Device for Sensitive Detection of Pathogenic Bacteria. *Small* **14**, e1801893 (2018).

35. Kong, T. *et al.* Accessory-free quantitative smartphone imaging of colorimetric paper-based assays. *Lab Chip* **19**, 1991–1999 (2019).

36. AbdelFatah, T., Jalali, M. & Mahshid, S. Multifunctional nanofilter for fluidic devices by pillar-assisted self-assembly microparticles. *Biomicrofluidics* (2018).

37. Hirsch, M. *et al.* ZnO coated fiber optic microsphere sensor for the enhanced refractive index sensing. *Sensors Actuators, A Phys.* **298**, (2019).

38. Steinberg, P. High-throughput screening methods in toxicity testing. Chapter 5 (2013).

39. Underwood, S. & Mulvaney, P. Effect of the Solution Refractive Index on the Color of Gold Colloids. *Langmuir* **10**, 3427–3430 (1994).

40. Rezaei, S. D., Ho, J., Ng, R. J. H., Ramakrishna, S. & Yang, J. K. W. On the correlation of absorption cross-section with plasmonic color generation. *Opt. Express* **25**, 27652–27664 (2017).

41. Bohren, C. F. & Huffman, D. R. *Absorption and scattering of light by small particles*. (Wiley, 1983).

42. Wang, L. *et al.* Large Area Plasmonic Color Palettes with Expanded Gamut Using Colloidal Self-Assembly. *ACS Photonics* **3**, 627–633 (2016).

43. Wu, H. Y., Choi, C. J. & Cunningham, B. T. Plasmonic nanogap-enhanced raman scattering using a resonant nanodome array. *Small* **8**, 2878–2885 (2012).

44. Wu, H. Y., Choi, C. J. & Cunningham, B. T. Plasmonic nanogap-enhanced Raman scattering using a resonant nanodome array. *Small* **8**, 2878–2885 (2012).

45. Pivetal, J., Woodward, M. J., Reis, N. M. & Edwards, A. D. High Dynamic Range Bacterial Cell Detection in a Novel " Lab -In-A- Comb " f or High-Throughput Antibiotic Susceptibility Testing of Clinical Urine Samples. (2017).

46. Hou, Z. *et al.* Time lapse investigation of antibiotic susceptibility using a microfluidic linear gradient 3D culture device. *Lab Chip* **14**, 3409–3418 (2014).

47. Sandberg, M. E. *et al.* Pros and cons of using resazurin staining for quanti fi cation of viable Staphylococcus aureus bio fi lms in a screening assay. *J. Microbiol. Methods* **78**, 104–106 (2009).

48. Mariscal, A., Lopez-gigosos, R. M., Carnero-varo, M. & Fernandez-crehuet, J. Fluorescent assay based on resazurin for detection of activity of disinfectants against bacterial biofilm. 773–783 (2009). doi:10.1007/s00253-009-1879-x

49. Clinical and Laboratory Standards Institute. *Performance standards for antimibrobial susceptibility testing. Nineteenth informational supplement. Approved standard M100-S20*. *Clinical and Laboratory Standards Institute: Wayne, PA.* (2010).

50. Mancini, S. *et al.* Population-based inference of aminoglycoside resistance mechanisms in Escherichia coli. *EBioMedicine* **46**, 184–192 (2019).

51. Carter, E. C. *et al. CIE 15:2018 "Colorimetry, 4th Edition"*. (2018). doi:10.25039/TR.015.2018

4. Summary and Conclusion

A Plasmonic-Enhanced Lab-on-a-Chip Device for Bacteria Drug Susceptibility was developed. The device meets the current need for rapid colorimetric point of care drug susceptibility screening tests. First, a filter element was developed for efficient bacteria capture. It depends on the interaction between Polystyrene particles and micropillar array. An optimization study was carried out to determine the design for efficient accumulation of Polystyrene particles and formation of a filter element. The micropillar array design featuring 10 μm inter-pillar spacing was the optimum design with the highest PSP capture capability (58.8%). The formation of the filter element was investigated experimentally using fluorescently tagged PSP and the bacteria capture was evaluated using fluorescently tagged *E Coli* bacteria. Next, a plasmonic enhanced Lab-on-a-chip device was developed for screening for Bacteria Drug Susceptibility. The design incorporated a bacteria capture chamber with a PSP/pillar filter element for bacteria confinement. The design introduced a color reading chamber with an integrated plasmonic metasurface platform for sensitive detection of color change. The plasmonic platform consisted of a self-assembled monolayer of 400 nm diameter polystyrene nanoparticles, Zinc oxide spacer layer, and Aluminum layer. The device utilized the metabolic reduction of dark blue resazurin to pink resorufin by viable cells as an indicator of antibiotic efficacy. The plasmonic platform allowed for sensitive detection of color change thus reducing the time required for sample incubation and enabling rapid screening. Color change collaborated to resistant behavior was detected after 30 minutes and 1 hour for E Coli concentrations of 10^{05} CFU/mL and 100 CFU/mL respectively. Moreover, the minimum inhibitory concentration of kanamycin was evaluated by both the plasmonic platform and standard protocol and was within the acceptable 2-fold variation (8 μg/mL and 4 μg/mL respectively). The future work for the device is expanding its application range. An interesting venue is screening for drug efficacy against other pathogens. Resazurin assays have been used with fungus, viruses, or worms. This device will allow faster detection time and a cheaper overall cost. Another promising application is the integration of molecular diagnostics for colorimetric pathogen identification. This integration would introduce a powerful point of care molecular diagnostics kit as the device does not require sophisticated equipment for operation. All in all, an integrated microfluidic device for bacterial capture and antimicrobial screening was developed. It incorporated a flexible colorimetric plasmonic readout platform suitable for application in low resource settings

Appendix A "plasmonic Lab-on-a-chip fabrication and characterization"

Here we discuss the fabrication procedure of the developed plasmonic enhanced Lab-on-a-chip device. Figure (A.1) shows the workflow for fabricating the plasmonic enhanced microfluidic Lab-on-a-chip device. First, a silicon wafer is washed with DI water, blown dry with a nitrogen gun. Consequently, the wafer is spin-coated with the negative photoresist SU-8 2015 and soft baked at 95℃ for 3 minutes (figures A.1a-b). Next, the device design is patterned using a UV mask aligner and the design mask. The exposed wafer is subsequently developed with SU-8 developer (figure A.1c-d). The self-assembled monolayer of nanoparticles if formed using a generic approach at the water/air interface which is selectively patterned to the color reading chamber upon the drying of the water droplet (figures A.1h-g). The following step includes ZnO (60 nm) and Aluminum (15 nm) deposition using a BJD 1800 e-beam evaporator (figures A.1f-g). Last the device is sealed using a cured PDMS slap which is punshed for interfacing. The PDMS slap is put in contact with a thin layer of freshly mixed PDMS solution, then put in contact with the device with no applied pressure and left to dry at room temperature for 48 hours (figures A.1i-k).

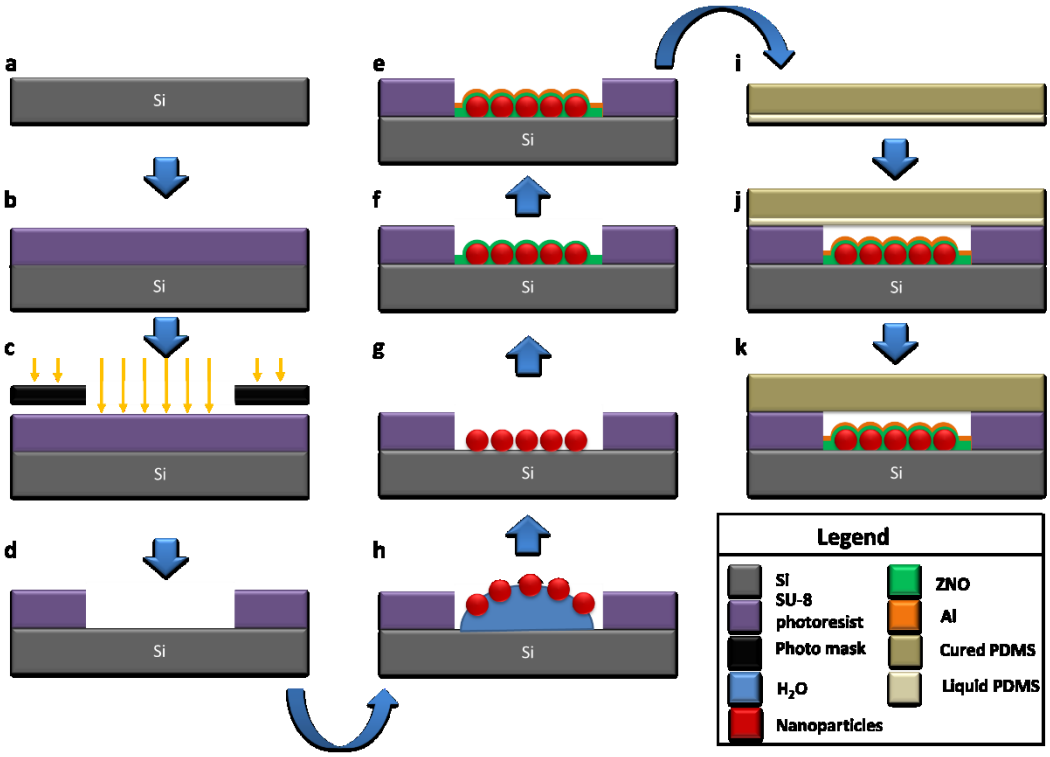

Figure A. 1 Fabrication flow for the plasmonic enhanced Lab-on-a-chip microfluidic device.

For the characterization study silicon pieces with the self-assembled monolayer (SAM) of nanoparticles of different sizes (200 nm, 400 nm, 600 nm, 750 nm, and 1000 nm) were used. The silicon pieces with SAM were subsequently deposited with 60nm and 15nm of ZnO and Al layers respectively. Tapping mode atomic force microscopy (AFM) was performed to characterize the morphology of different plasmonic platforms. Figure (A.2) shows the structure of the ZnO/Al deposited self-assembled monolayer of nanoparticles. The nanoparticles are arranged in a tight hexagonal packing structure. Figures (A.2 a-e) show the layer structure for the SAM layers with 200 nm, 400 nm, 600 nm, 750 nm, and 1000 nm diameter nanoparticles respectively. The interparticle gap spacing can be considered to act as vertical plasmonic nanocavity. The interparticle gap length is increased from 73 nm to 340 nm with increasing nanoparticle diameter of the SAM layer from 200 nm to 1000 nm. A study was performed to compare the sensitivity of platforms with different SAM layers to detect color change. The different platforms were challenged with aliquots of resazurin mixed with 10^5 CFU/mL E. coli bacteria and incubated at 37℃ for different time durations from 5 to 60 minutes with 5 minutes time step. The reflectance spectra of the different plasmonic platforms with droplets of the aliquots were measured as shown in Figure (A.3). All platforms exhibited a lattice resonance dip at a shorter wavelength (~ 405nm) which didn't exhibit shifting with different aliquots. A high order resonance dip is witnessed at longer wavelengths. As the resazurin is reduced to resorufin by viable bacteria a gradual blue shift is witnessed in the high order resonance dip. Different platforms had different dip shifts as shown in Table A-1. The 200 nm, 600 nm, and 1000 nm plasmonic platforms exhibited low sensitivity with small dip shifts of 2.5 nm, 3 nm, and 2 nm respectively. On contrast, the 400 nm and 750 nm platforms showed more sensitive detection of the color change with dip shifts of 37 nm and 26 nm respectively. The 400 nm platform showed the most spectral sensitivity towards detecting the color change during the reduction of resazurin to resorufin.

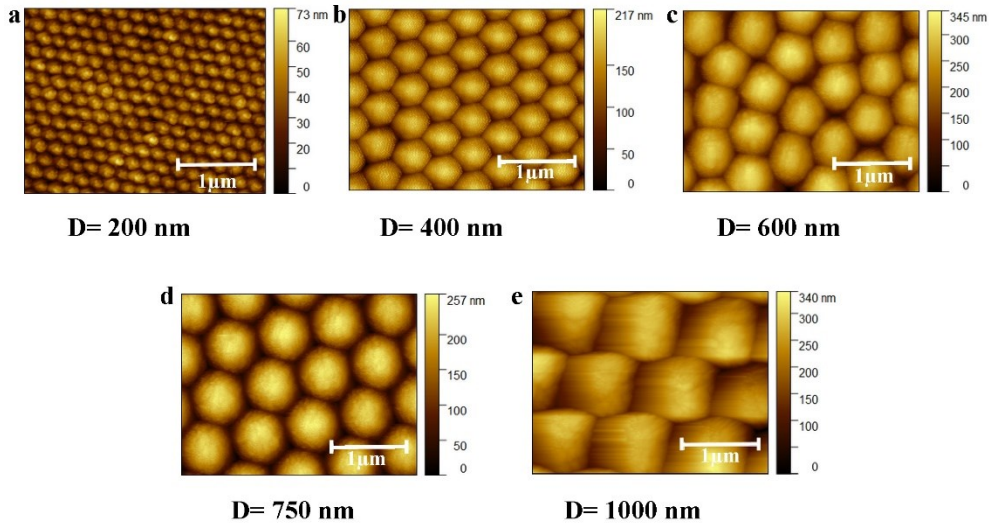

Figure A. 2 Atomic force microscopy characterization of plasmonic platforms

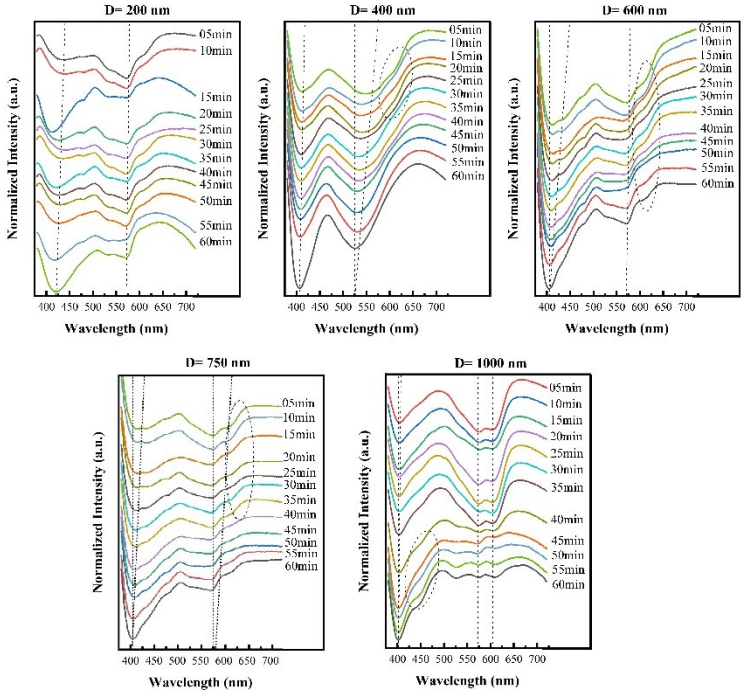

Figure A. 3 plasmonic platform optimization study.

Table A- 1 Dip position shift ($\Delta\lambda_{Dip}$) for different plasmonic platforms

SAM particle diameter	D= 200 nm	D= 400 nm	D= 600 nm	D= 750 nm	D= 1000 nm
Dip shift (nm)	2.5	37	3	26	2

Master Bibliography

1. Introduction and literature review

1. Rossolini, G. M., Arena, F., Pecile, P. & Pollini, S. Update on the antibiotic resistance crisis. *Curr. Opin. Pharmacol.* **18**, 56–60 (2014).

2. Ventola, C. L. The antibiotic resistance crisis: part 1: causes and threats. *Pharm. Ther. J.* **40**, 277–83 (2015).

3. Sprenger, M. & Fukuda, K. New mechanisms, new worries. *Science (80-.).* **351**, 1263 LP – 1264 (2016).

4. World Health Organization. *Global action plan on antimicrobial resistance*. (2015).

5. Tornimbene, B. *et al. WHO Global Antimicrobial Resistance Surveillance System early implementation 2016–17*. *The Lancet Infectious Diseases* **18**, (2018).

6. Ventola, C. L. The antibiotic resistance crisis: part 2: management strategies and new agents. *P T* **40**, 344–352 (2015).

7. Lushniak, B. D. Antibiotic resistance: a public health crisis. *Public Health Rep.* **129**, 314–316 (2014).

8. Bartlett, J. G., Gilbert, D. N. & Spellberg, B. Seven Ways to Preserve the Miracle of Antibiotics. *Clin. Infect. Dis.* **56**, 1445–1450 (2013).

9. Michael, C. A., Dominey-Howes, D. & Labbate, M. The antimicrobial resistance crisis: causes, consequences, and management. *Front. public Heal.* **2**, 145 (2014).

10. *CLSI. Methods for Dilution Antimicrobial Susceptibility Tests f or Bacteria That Grow Aerobically; Approved St andard—Ninth Edition.* (2012).

11. Organization, W. H. *Manual for the laboratory identification and antimicrobial susceptibility testing of bacterial pathogens of public health importance in the developing world: Haemophilus influenzae, Neisseria meningitidis, Streptococcus pneumoniae, Neisseria gonorrhoea, S.* (Geneva: World Health Organization, 2003).

12. Papan, C. *et al.* Assessment of the multiplex PCR-based assay Unyvero pneumonia application for detection of bacterial pathogens and antibiotic resistance genes in children and neonates. *Infection* **46**, 189–196 (2018).

13. Redondo, J. J., Keller, P. M., Zbinden, R. & Wagner, K. A novel RT-PCR for the detection of Helicobacter pylori and identification of clarithromycin resistance mediated by mutations in the 23S rRNA gene. *Diagn. Microbiol. Infect. Dis.* **90**, 1–6 (2018).

14. Maxson, T., Blancett, C. D., Graham, A. S., Stefan, C. P. & Minogue, T. D. Rapid antibiotic susceptibility testing from blood culture bottles with species agnostic real-time

polymerase chain reaction. *PLoS One* **13**, e0209042–e0209042 (2018).

15. Alame-Emane, A. K. *et al.* Use of GeneXpert Remnants for Drug Resistance Profiling and Molecular Epidemiology of Tuberculosis in Libreville, Gabon. *J. Clin. Microbiol.* **55**, 2105–2115 (2017).

16. Özcan, N., Akpolat, N., Atmaca, S. & Gül, K. GeneXpert vanA / vanB test and culture method in evaluation of Vancomycin Resistant Enterococcus (VRE) colonisation in a tertiary hospital. **10**, 33–39 (2018).

17. Opollo, V. S. *et al.* Field evaluation of near point of care Cepheid GeneXpert HIV-1 Qual for early infant diagnosis. *PLoS One* **13**, e0209778 (2018).

18. Fitzpatrick, M. B. *et al.* hrHPV prevalence and type distribution in rural Zimbabwe: A community-based self-collection study using near-point-of-care GeneXpert HPV testing. *Int. J. Infect. Dis.* **82**, 21–29 (2019).

19. Obioma, A., Ngozika, W. G. & Appollus, J. N. Evidence-based comparison of molecular-genexpert and microscopic method in the diagnosis of mycobacteriumtuberculosisamong subjects in the limited resource setting of Niger delta. *J. Microbiol. Exp.* **6**, 98–102 (2018).

20. Besant, J. D., Sargent, E. H. & Kelley, S. O. Rapid electrochemical phenotypic profiling of antibiotic-resistant bacteria. *Lab Chip* **15**, 2799–2807 (2015).

21. Kelley, S. O. New Technologies for Rapid Bacterial Identification and Antibiotic Resistance Profiling. *SLAS Technol.* **22**, 113–121 (2017).

22. Webster, T. A., Sismaet, H. J., Chan, I. P. J. & Goluch, E. D. Electrochemically monitoring the antibiotic susceptibility of Pseudomonas aeruginosa biofilms. *Analyst* **140**, 7195–7201 (2015).

23. Riss, T. L. & Moravec, R. A. Chapter 4 - Cell Proliferation Assays: Improved Homogeneous Methods Used to Measure the Number of Cells in Culture. in (ed. Celis, J. E. B. T.-C. B. (Third E.) 25–31 (Academic Press, 2006). doi:https://doi.org/10.1016/B978-012164730-8/50005-8

24. Chen, J. L., Steele, T. W. J. & Stuckey, D. C. Metabolic reduction of resazurin; location within the cell for cytotoxicity assays. *Biotechnol. Bioeng.* **115**, 351–358 (2018).

25. Kaushik, A. M. *et al.* Accelerating bacterial growth detection and antimicrobial susceptibility assessment in integrated picoliter droplet platform. *Biosens. Bioelectron.* **97**, 260–266 (2017).

26. Reis, N. M., Pivetal, J., Loo-Zazueta, A. L., Barros, J. M. S. & Edwards, A. D. Lab on a stick: multi-analyte cellular assays in a microfluidic dipstick. *Lab Chip* **16**, 2891–2899 (2016).

27. Elavarasan, T., Chhina, S. K., Parameswaran (Ash), M. & Sankaran, K. Resazurin reduction based colorimetric antibiogram in microfluidic plastic chip. *Sensors Actuators B Chem.* **176**, 174–180 (2013).

28. Dreaden, E. C., Alkilany, A. M., Huang, X., Murphy, C. J. & El-Sayed, M. A. The golden age: Gold nanoparticles for biomedicine. *Chem. Soc. Rev.* **41**, 2740–2779 (2012).

29. Si, G. *et al.* Reflective plasmonic color filters based on lithographically patterned silver nanorod arrays. *Nanoscale* **5**, 6243–6248 (2013).

30. Wang, L. *et al.* Large Area Plasmonic Color Palettes with Expanded Gamut Using Colloidal Self-Assembly. *ACS Photonics* **3**, 627–633 (2016).

31. Gu, Y., Zhang, L., Yang, J. K. W., Yeo, S. P. & Qiu, C. W. Color generation via subwavelength plasmonic nanostructures. *Nanoscale* **7**, 6409–6419 (2015).

32. Kumar, K. *et al.* Printing colour at the optical diffraction limit. *Nat. Nanotechnol.* **7**, 557–561 (2012).

33. Duan, H., Hu, H., Kumar, K., Shen, Z. & Yang, J. K. W. Direct and reliable patterning of plasmonic nanostructures with sub-10-nm gaps. *ACS Nano* **5**, 7593–7600 (2011).

34. Innocenzi, P. *et al.* Hierarchical Mesoporous Films : From Self-Assembly to Porosity with Different Length Scales. 2501–2509 (2011). doi:10.1021/cm200050r

35. Zhang, B. J., Li, Y., Zhang, X. & Yang, B. Colloidal Self-Assembly Meets Nanofabrication : From Two- Dimensional Colloidal Crystals to Nanostructure Arrays. **130012**, 4249–4269 (2010).

36. Yokogawa, S., Burgos, S. P. & Atwater, H. A. Plasmonic color filters for CMOS image sensor applications. *Nano Lett.* **12**, 4349–4354 (2012).

37. Goh, X. M. *et al.* Three-dimensional plasmonic stereoscopic prints in full colour. *Nat. Commun.* **5**, 1–8 (2015).

2. A nanofilter for fluidic devices by pillar-assisted self-assembly microparticles

1. Li, M. *et al.* Simultaneous detection of four different neuraminidase types of avian influenza A H5 viruses by multiplex reverse transcription PCR using a GeXP analyser. *Influenza Other Respi. Viruses* **10**, 141–149 (2016).
2. Teoh, B. T. *et al.* The Use of NS1 Rapid Diagnostic Test and qRT-PCR to Complement IgM ELISA for Improved Dengue Diagnosis from Single Specimen. *Sci. Rep.* **6**, 1–8 (2016).
3. Wagenlehner, F. M. E., Pilatz, A. & Weidner, W. Urosepsis - From the view of the urologist. *Int. J. Antimicrob. Agents* **38**, 51–57 (2011).
4. Abdulwahab, S. *et al.* Towards a personalized approach to aromatase inhibitor therapy: a digital microfluidic platform for rapid analysis of estradiol in core-needle-biopsies. *Lab Chip* **17**, 1594–1602 (2017).
5. Gnyawali, V., Saremi, M., Kolios, M. C. & Tsai, S. S. H. Stable microfluidic flow focusing using hydrostatics. *Biomicrofluidics* **11**, (2017).
6. Ghaemi, R., Rezai, P., Nejad, F. R. & Selvaganapathy, P. R. Characterization of

microfluidic clamps for immobilizing and imaging of Drosophila melanogaster larva's central nervous system. *Biomicrofluidics* **11**, (2017).
7. Besant, J. D., Sargent, E. H. & Kelley, S. O. Rapid electrochemical phenotypic profiling of antibiotic-resistant bacteria. *Lab Chip* **15**, 2799–2807 (2015).
8. Mahshid, S. *et al.* Development of a platform for single cell genomics using convex lens-induced confinement. *Lab Chip* **15**, 3013–20 (2015).
9. Zhao, C., Ge, Z. & Yang, C. Microfluidic Techniques for Analytes Concentration. *Micromachines* **8**, 28 (2017).
10. Hamada, R. *et al.* A rapid bacteria detection technique utilizing impedance measurement combined with positive and negative dielectrophoresis. *Sensors Actuators, B Chem.* **181**, 439–445 (2013).
11. Puchberger-Enengl, D. *et al.* Microfluidic concentration of bacteria by on-chip electrophoresis. *Biomicrofluidics* **5**, (2011).
12. Zhang, W. & Radadia, A. D. Toward a Boron-Doped Ultrananocrystalline Diamond Electrode-Based Dielectrophoretic Preconcentrator. *Anal. Chem.* **88**, 2605–2613 (2016).
13. Mahshid, S. *et al.* Transverse dielectrophoretic-based DNA nanoscale confinement. *Sci. Rep.* **8**, 1–12 (2018).
14. Islam, S. *et al.* Electrophoretic Concentration and Electrical Lysis of Bacteria in a Microfluidic Device Using a Nanoporous Membrane. (2017). doi:10.3390/mi8020045
15. Qiao, W. *et al.* A two-stage electrophoretic microfluidic device for nucleic acid collection and enrichment. *Microfluid. Nanofluidics* **20**, 1–9 (2016).
16. Madiyar, F. R., Syed, L. U., Arumugam, P. & Li, J. Electrical capture and detection of microbes using dielectrophoresis at nanoelectrode arrays. in *ACS Symposium Series* **1143**, 109–124 (2013).
17. del Moral Zamora, B. *et al.* Dielectrophoretic concentrator enhancement based on dielectric poles for continuously flowing samples. *Electrophoresis* **36**, 1405–1413 (2015).
18. del Moral-Zamora, B. *et al.* Combined dielectrophoretic and impedance system for on-chip controlled bacteria concentration: Application to Escherichia coli. *Electrophoresis* **36**, 1130–1141 (2015).
19. Yan, H. *et al.* Multiplex detection of bacteria on an integrated centrifugal disk using bead-beating lysis and loop-mediated amplification. *Sci. Rep.* **7**, 1–11 (2017).
20. Wiederoder, M. S. *et al.* Novel functionalities of hybrid paper-polymer centrifugal devices for assay performance enhancement. *Biomicrofluidics* **11**, (2017).
21. Chen, Y. Y. *et al.* Corona-induced micro-centrifugal flows for concentration of Neisseria and Salmonella bacteria prior to their quantitation using antibody-functionalized SERS-reporter nanobeads. *Microchim. Acta* **184**, 1021–1028 (2017).
22. Li, H.-Y. *et al.* Micropillar array chips toward new immunodiagnosis. *Lab Chip* **10**, 2597–604 (2010).
23. Tsougeni, K. *et al.* Plasma nanotextured polymeric lab-on-a-chip for highly efficient bacteria capture and lysis. *Lab Chip* **16**, 120–131 (2016).
24. Wang, R. *et al.* Immuno-capture and in situ detection of Salmonella typhimurium on a novel microfluidic chip. *Anal. Chim. Acta* **853**, 710–717 (2015).
25. Jalali, M. *et al.* A Hierarchical 3D Nanostructured Microfluidic Device for Sensitive Detection of Pathogenic Bacteria. *Small* 1801893 (2018). doi:10.1002/smll.201801893
26. Chang, C. H. & Yang, R. J. Enhanced sample preconcentration in microfluidic chip using graphene oxide–Nafion membrane. *Microfluid. Nanofluidics* **20**, 1–9 (2016).

27. Tian, F., Lyu, J., Shi, J., Tan, F. & Yang, M. A polymeric microfluidic device integrated with nanoporous alumina membranes for simultaneous detection of multiple foodborne pathogens. *Sensors Actuators, B Chem.* **225**, 312–318 (2016).
28. Ahamed, M. J. *et al.* Continuous Confinement Fluidics: Getting Lots of Molecules into Small Spaces with High Fidelity. *Macromolecules* **49**, 2853–2859 (2016).
29. Zimny, P., Juncker, D. & Reisner, W. Hydrogel droplet single-cell processing: DNA purification, handling, release, and on-chip linearization. *Biomicrofluidics* **12**, (2018).
30. Feng, S. L., Skelley, A. M., Anwer, A. G., Liu, G. & Inglis, D. W. Maximizing particle concentration in deterministic lateral displacement arrays. *Biomicrofluidics* **11**, (2017).
31. Holm, Stefan H.; Beech, Jason P.; Barrett, Michael P.; Tegenfeldt, J. O. Separation of parasites from human blood using deterministic lateral displacement †. *Lab Chip* 1326–1332 (2011). doi:10.1039/c0lc00560f
32. Huang, L. R., Cox, E. C., Austin, R. H. & Sturm, J. C. Continous particle separation through deterministic lateral displacement. *Science (80-.).* **304**, 987–991 (2004).
33. Zhang, Z., Zhao, P., Xiao, G., Watts, B. R. & Xu, C. Sealing SU-8 microfluidic channels using PDMS. *Biomicrofluidics* **5**, (2011).
34. Dai, Z., Li, Y., Duan, G., Jia, L. & Cai, W. Phase Diagram , Design of Monolayer Binary Colloidal Crystals , and Their Fabrication Based on Ethanol-Assisted Self-Assembly at the Air / Water Interface. *ACS Nano* 6706–6716 (2012). doi:10.1021/nn3013178
35. Nagy, A. & Gaspar, A. Packed multi-channels for parallel chromatographic separations in microchips. *J. Chromatogr. A* **1304**, 251–256 (2013).
36. Beech, Jason P.; Tegenfeldt, J. O. Microfluidics Separation and Analysis of Biological Particles. (Lund university, 2011).
37. McGrath, J., Jimenez, M. & Bridle, H. Deterministic lateral displacement for particle separation: A review. *Lab on a Chip* **14**, 4139–4158 (2014).
38. Ceriotti, L., De Rooij, N. F. & Verpoorte, E. An integrated fritless column for on-chip capillary electrochromatography with conventional stationary phases. *Anal. Chem.* **74**, 639–647 (2002).
39. Greenwood, R., Luckham, P. F. & Gregory, T. The effect of diameter ratio and volume ratio on the viscosity of bimodal suspensions of polymer latices. *J. Colloid Interface Sci.* **191**, 11–21 (1997).
40. Asmolov, E. S., Dubov, A. L., Nizkaya, T. V., Harting, J. & Vinogradova, O. I. Inertial focusing of finite-size particles in microchannels. *J. Fluid Mech.* **840**, 613–630 (2018).

3. Plasmonic-Enhanced Lab-on-a-Chip Device for Bacteria Drug Susceptibility (Under preparation).

1. Ventola, C. L. The antibiotic resistance crisis: part 1: causes and threats. *Pharm. Ther. J.* **40**, 277–83 (2015).

2. Spellberg, B. & Gilbert, D. N. The future of antibiotics and resistance: a tribute to a career of leadership by John Bartlett. *Clin. Infect. Dis.* **59 Suppl 2**, S71–S75 (2014).

3. Ventola, C. L. The antibiotic resistance crisis: part 2: management strategies and new

agents. *P T* **40**, 344–352 (2015).

4. Organization, W. H. *Manual for the laboratory identification and antimicrobial susceptibility testing of bacterial pathogens of public health importance in the developing world: Haemophilus influenzae, Neisseria meningitidis, Streptococcus pneumoniae, Neisseria gonorrhoea, S*. (Geneva: World Health Organization, 2003).

5. *CLSI. Methods for Dilution Antimicrobial Susceptibility Tests f or Bacteria That Grow Aerobically; Approved St andard—Ninth Edition.* (2012).

6. Maxson, T., Blancett, C. D., Graham, A. S., Stefan, C. P. & Minogue, T. D. Rapid antibiotic susceptibility testing from blood culture bottles with species agnostic real-time polymerase chain reaction. *PLoS One* **13**, e0209042–e0209042 (2018).

7. Whiley, D. M. *et al.* Molecular Antimicrobial Resistance Surveillance for Neisseria gonorrhoeae, Northern Territory, Australia. *Emerg. Infect. Dis.* **23**, 1478–1485 (2017).

8. Vatanshenassan, M. *et al.* Proof of Concept for MBT ASTRA, a Rapid Matrix-Assisted Laser Desorption Ionization–Time of Flight Mass Spectrometry (MALDI-TOF MS)-Based Method To Detect Caspofungin Resistance in <span class="named-content genus-species" id="named-cont. *J. Clin. Microbiol.* **56**, e00420-18 (2018).

9. Elshikh, M. *et al.* Resazurin-based 96-well plate microdilution method for the determination of minimum inhibitory concentration of biosurfactants. *Biotechnol. Lett.* **38**, 1015–1019 (2016).

10. Sun, H. *et al.* Reliable and reusable whole polypropylene plastic microfluidic devices for a rapid, low-cost antimicrobial susceptibility test. *Lab Chip* **19**, 2915–2924 (2019).

11. Manz, A. *et al.* Planar chips technology for miniaturization and integration of separation techniques into monitoring systems: Capillary electrophoresis on a chip. *J. Chromatogr. A* **593**, 253–258 (1992).

12. Maguire, I., O'Kennedy, R., Ducrée, J. & Regan, F. A review of centrifugal microfluidics in environmental monitoring. *Anal. Methods* **10**, 1497–1515 (2018).

13. Kelley, S. O. New Technologies for Rapid Bacterial Identification and Antibiotic Resistance Profiling. *SLAS Technol.* **22**, 113–121 (2017).

14. Lyu, F. *et al.* Phenotyping antibiotic resistance with single-cell resolution for the detection of heteroresistance. *Sensors Actuators, B Chem.* **270**, 396–404 (2018).

15. Abbaspourrad, A. *et al.* Nanoliter-Sized Microchamber/Microarray Microfluidic Platform for Antibiotic Susceptibility Testing. *Anal. Chem.* **90**, 14137–14144 (2018).

16. Elavarasan, T., Chhina, S. K., Parameswaran (Ash), M. & Sankaran, K. Resazurin reduction based colorimetric antibiogram in microfluidic plastic chip. *Sensors Actuators B Chem.* **176**, 174–180 (2013).

17. Lee, W.-B. *et al.* A microfluidic device for antimicrobial susceptibility testing based on a

broth dilution method. *Biosens. Bioelectron.* **87**, 669–678 (2017).

18. Jalali, M. *et al.* Stacking of colors in exfoliable plasmonic superlattices. *Nanoscale* **8**, 18228–18234 (2016).

19. Dreaden, E. C., Alkilany, A. M., Huang, X., Murphy, C. J. & El-Sayed, M. A. The golden age: Gold nanoparticles for biomedicine. *Chem. Soc. Rev.* **41**, 2740–2779 (2012).

20. Si, G. *et al.* Reflective plasmonic color filters based on lithographically patterned silver nanorod arrays. *Nanoscale* **5**, 6243–6248 (2013).

21. Wang, L. *et al.* Large Area Plasmonic Color Palettes with Expanded Gamut Using Colloidal Self-Assembly. *ACS Photonics* **3**, 627–633 (2016).

22. Halas, N. J., Lal, S., Chang, W. S., Link, S. & Nordlander, P. Plasmons in strongly coupled metallic nanostructures. *Chem. Rev.* **111**, 3913–3961 (2011).

23. Gu, Y., Zhang, L., Yang, J. K. W., Yeo, S. P. & Qiu, C. W. Color generation via subwavelength plasmonic nanostructures. *Nanoscale* **7**, 6409–6419 (2015).

24. Kumar, K. *et al.* Printing colour at the optical diffraction limit. *Nat. Nanotechnol.* **7**, 557–561 (2012).

25. Duan, H., Hu, H., Kumar, K., Shen, Z. & Yang, J. K. W. Direct and reliable patterning of plasmonic nanostructures with sub-10-nm gaps. *ACS Nano* **5**, 7593–7600 (2011).

26. F. Watt, A.A. Betiol, J.A. Van Kan, E. J. T. and M. B. . B. ION BEAM LITHOGRAPHY AND NANOFABRICATION : Next generation lithographies (NGLs) are being actively developed to take over from the highly successful optical lithography . As feature sizes shrink well below 100 nm , several key challenges for optical lit. *Int. J. Nanosci.* **4**, 269–286 (2005).

27. Innocenzi, P. *et al.* Hierarchical Mesoporous Films : From Self-Assembly to Porosity with Different Length Scales. 2501–2509 (2011). doi:10.1021/cm200050r

28. Zhang, B. J., Li, Y., Zhang, X. & Yang, B. Colloidal Self-Assembly Meets Nanofabrication : From Two- Dimensional Colloidal Crystals to Nanostructure Arrays. **130012**, 4249–4269 (2010).

29. Yokogawa, S., Burgos, S. P. & Atwater, H. A. Plasmonic color filters for CMOS image sensor applications. *Nano Lett.* **12**, 4349–4354 (2012).

30. Goh, X. M. *et al.* Three-dimensional plasmonic stereoscopic prints in full colour. *Nat. Commun.* **5**, 1–8 (2015).

31. Riss, T. L. & Moravec, R. A. Chapter 4 - Cell Proliferation Assays: Improved Homogeneous Methods Used to Measure the Number of Cells in Culture. in (ed. Celis, J. E. B. T.-C. B. (Third E.) 25–31 (Academic Press, 2006). doi:https://doi.org/10.1016/B978-012164730-8/50005-8

32. Chen, J. L., Steele, T. W. J. & Stuckey, D. C. Metabolic reduction of resazurin; location

within the cell for cytotoxicity assays. *Biotechnol. Bioeng.* **115**, 351–358 (2018).

33. Gajasinghe, R. W. R. L. *et al.* Experimental study of PDMS bonding to various substrates for monolithic microfluidic applications. *J. Micromechanics Microengineering* **24**, 75010 (2014).

34. Jalali, M. *et al.* A Hierarchical 3D Nanostructured Microfluidic Device for Sensitive Detection of Pathogenic Bacteria. *Small* **14**, e1801893 (2018).

35. Kong, T. *et al.* Accessory-free quantitative smartphone imaging of colorimetric paper-based assays. *Lab Chip* **19**, 1991–1999 (2019).

36. AbdelFatah, T., Jalali, M. & Mahshid, S. Multifunctional nanofilter for fluidic devices by pillar-assisted self-assembly microparticles. *Biomicrofluidics* (2018).

37. Hirsch, M. *et al.* ZnO coated fiber optic microsphere sensor for the enhanced refractive index sensing. *Sensors Actuators, A Phys.* **298**, (2019).

38. Steinberg, P. High-throughput screening methods in toxicity testing. Chapter 5 (2013).

39. Underwood, S. & Mulvaney, P. Effect of the Solution Refractive Index on the Color of Gold Colloids. *Langmuir* **10**, 3427–3430 (1994).

40. Rezaei, S. D., Ho, J., Ng, R. J. H., Ramakrishna, S. & Yang, J. K. W. On the correlation of absorption cross-section with plasmonic color generation. *Opt. Express* **25**, 27652–27664 (2017).

41. Bohren, C. F. & Huffman, D. R. *Absorption and scattering of light by small particles*. (Wiley, 1983).

42. Wang, L. *et al.* Large Area Plasmonic Color Palettes with Expanded Gamut Using Colloidal Self-Assembly. *ACS Photonics* **3**, 627–633 (2016).

43. Wu, H., Choi, C. J. & Cunningham, B. T. full papers Plasmonic Nanogap-Enhanced Raman Scattering Using a Resonant Nanodome Array. 2878–2885 (2012). doi:10.1002/smll.201200712

44. Wu, H. Y., Choi, C. J. & Cunningham, B. T. Plasmonic nanogap-enhanced Raman scattering using a resonant nanodome array. *Small* **8**, 2878–2885 (2012).

45. Pivetal, J., Woodward, M. J., Reis, N. M. & Edwards, A. D. High Dynamic Range Bacterial Cell Detection in a Novel " Lab -In-A- Comb " f or High-Throughput Antibiotic Susceptibility Testing of Clinical Urine Samples. (2017).

46. Hou, Z. *et al.* Time lapse investigation of antibiotic susceptibility using a microfluidic linear gradient 3D culture device. *Lab Chip* **14**, 3409–3418 (2014).

47. Sandberg, M. E. *et al.* Pros and cons of using resazurin staining for quanti fi cation of viable Staphylococcus aureus bio fi lms in a screening assay. *J. Microbiol. Methods* **78**, 104–106 (2009).

48. Mariscal, A., Lopez-gigosos, R. M., Carnero-varo, M. & Fernandez-crehuet, J. Fluorescent assay based on resazurin for detection of activity of disinfectants against bacterial biofilm. 773–783 (2009). doi:10.1007/s00253-009-1879-x

49. Clinical and Laboratory Standards Institute. *Performance standards for antimibrobial susceptibility testing. Nineteenth informational supplement. Approved standard M100-S20*. *Clinical and Laboratory Standards Institute: Wayne, PA.* (2010).

50. Mancini, S. *et al.* Population-based inference of aminoglycoside resistance mechanisms in Escherichia coli. *EBioMedicine* **46**, 184–192 (2019).

51. Carter, E. C. *et al. CIE 15:2018 "Colorimetry, 4th Edition"*. (2018). doi:10.25039/TR.015.2018